



Escola d'Enginyeria de Telecomunicació i
Aeroespacial de Castelldefels

UNIVERSITAT POLITÈCNICA DE CATALUNYA BARCELONATECH

MASTER THESIS

TITLE : Preliminary study of an innovative Non-Destructive Testing technique concept for detection of surface cracks in non-ferromagnetic materials

DEGREE: Master in Aerospace Science and Technology

AUTHOR: Blai Cabrera Añón

DIRECTOR: José Ignacio Rojas

DATE: 4th November 2013

Title : Preliminary study of an innovative Non-Destructive Testing technique concept for detection of surface cracks in non-ferromagnetic materials

Author: Blai Cabrera Añón

Director: José Ignacio Rojas

Date: 4th November 2013

Overview

The research presented in this thesis is framed in the preliminary study for the development of an innovative Non-Destructive Testing (NDT) technique concept based on deposition of a ferrofluid consisting of magnetic nanoparticles in the test-piece surface. The proposed technique is applicable to inspection of any type of materials except to ferromagnetic materials. Thus, it is specially suited to detect surface defects in a wide range of materials typically used in aerospace applications, i.e., non-ferromagnetic materials like aluminum alloys or composite materials like CFRP or GFRP.

The proposed technique aims at meeting the requirements of NDT end-users in the form of a significant reduction of surface inspection costs, as compared with the most commonly used techniques at present day, aside from visual inspection.

Keywords: innovative NDT technique, surface defects, ferrofluid, magnetic nanoparticles, non-ferromagnetic materials.

Títol : Preliminary study of an innovative Non-Destructive Testing technique concept for detection of surface cracks in non-ferromagnetic materials

Autor: Blai Cabrera Añón

Director: José Ignacio Rojas

Data: 4 de novembre de 2013

Resum

La investigació presentada en aquesta tesi s'emmarca en l'estudi preliminar d'un concepte innovador per al desenvolupament d'una tècnica d'assajos no destructius (NDT). Aquesta tècnica es basa en la deposició d'un ferrofluid format de nanopartícules magnètiques sobre la superfície de la peça de prova. La tecnologia proposada és aplicable per a la inspecció de qualsevol tipus de materials excepte els materials ferromagnètics. Així doncs, és especialment adequat per detectar defectes en la superfície d'una àmplia gamma de materials utilitzats típicament en aplicacions aeroespacials, és a dir, materials no ferromagnètics com són els aliatges d'alumini o materials compostos com els CFRP o els GFRP.

La tècnica proposada té com a objectiu el compliment dels requisits tècnics dels usuaris d'NDT aconseguint una reducció significativa dels costos d'inspecció, en comparació amb les tècniques més utilitzades en l'actualitat, a part de la inspecció visual.

Paraules clau: innovative NDT technique, surface defects, ferrofluid, magnetic nanoparticles, non-ferromagnetic materials.

I would like to publicly express my gratitude to Dr. José Ignacio Rojas for giving me the opportunity to perform this work at the *Universitat Politècnica de Catalunya (UPC-Barcelona Tech)* and supervising my progress during the preparation of the thesis; Dr. Daniel Crespo for his guidance, advice and ideas during the development of the project; Joshua Tristancho and Dr. Ramon Casanella for their technical advice. Finally, but most importantly, I would like to thank my family for their constant support over all these years.

CONTENTS

ABBREVIATIONS AND SYMBOLS	1
Abbreviations and Symbols	1
CHAPTER 1. Introduction	5
CHAPTER 2. Non-Destructive Testing	7
2.1. Classification of NDT methods	7
2.1.1. Surface techniques	8
2.1.2. Sub-surface techniques	10
2.2. Alternative and emerging techniques	12
2.3. NDT method selection	13
2.4. Global NDT equipment market estimates	13
2.4.1. Drivers	14
2.4.2. Trends and revenue forecasts	15
2.4.3. Recent activity	16
CHAPTER 3. Introduction to ferrofluids	17
3.1. Structure of ferrofluids	17
3.1.1. Surfacted ferrofluids	18
3.1.2. Ionic ferrofluids	18
3.2. Ferrofluid properties	19
3.3. Ferrofluid stability	25
3.4. Ferrofluid magnetization theory	27
3.4.1. Particle models	28
3.4.2. Magnetic relaxation theory	28
3.4.3. Equilibrium (DC) magnetization	30
3.4.4. Dynamic (AC) magnetization	32
CHAPTER 4. Magnetic Early Defect Detection	35
4.1. Experimental set	36

4.1.1. Magnetic fluid	36
4.1.2. Test specimen	36
4.1.3. Custom-made solenoid	38
4.1.4. Magnetometer	41
4.2. DC experiment set-up	42
4.3. AC experiment set-up	43
CHAPTER 5. Results and discussion	45
5.1. DC magnetization	45
5.2. AC magnetization	51
CHAPTER 6. Conclusions	55
6.1. Achieved objectives	55
6.2. Future Work	56
BIBLIOGRAPHY	57
APPENDIX A. Table of conversions	63
APPENDIX B. Specifications of the test specimen's AA	65
APPENDIX C. Initial and minimum detectable crack sizes	67
APPENDIX D. Custom-made solenoid for conducting tests	69
D.1. Blueprint and CAD of the solenoid	69
D.2. Pictures of the solenoid construction process	69
D.3. Analytical model for the DC magnetic field	69
D.4. Magnetic field under alternating current	76
APPENDIX E. Magnetometer specifications	79
E.1. Specifications	79
E.2. Probe orientation	79

E.3. Basic operation	80
E.4. Sensor calibration estimates	81

LIST OF FIGURES

2.1	Magnetic particle testing	9
2.2	Liquid penetrant testing procedure	9
2.3	Eddy current testing procedure	10
2.4	Radiography testing procedure	11
2.5	Sensitivity to crack orientation on radiography testing	11
2.6	Ultrasonic testing procedure	12
2.7	NDT method selection	14
2.8	Estimated NDT market share by industry in the 1990s	15
3.1	Sketch of surfacted ferrofluid grains	18
3.2	Sketch of ionic ferrofluid grains	18
3.3	Real and imaginary components of the dimensionless complex susceptibility as a function of $\Omega\tau$	24
3.4	Particle models and system of coordinates	28
3.5	Brownian relaxation compared to Néel relaxation	29
3.6	Contribution of the dipoles within a sphere to the net magnetization of a body	31
3.7	Dimensionless equilibrium magnetization as a function of Langevin parameter	32
3.8	AC magnetization of suspensions of ellipsoidal particles	33
4.1	MEDD experimental set	36
4.2	Test specimen with simulated crack	38
4.3	Example of a radially thick, multilayered solenoid	38
4.4	CAD of the custom-made solenoid	39
4.5	Magnetic field produced by a wire	40
4.6	Magnetic field produced by a solenoid	40
4.7	Magnetic field distribution along the solenoid revolution axis	40
4.8	Comparison between theoretical and measured DC magnetic field for the coil #1	41
4.9	AC magnetic field as a function of the frequency	41
4.10	MEDD DC experimental set-up: Hall sensor position with respect to the ferrofluid	42
4.11	MEDD AC experimental set-up: Hall sensor position with respect to the ferrofluid	44
5.1	Models of the test-piece and equivalent cylindrical magnetic dipole	46
5.2	Magnetization of a magnetic dipole as a result of an external magnetic field	47
5.3	Ferrofluid cylinder in a magnetic field	47
5.4	Non-dimensional magnetization as a function of the applied magnetic field	49
5.5	Dimensional magnetization as a function of the applied magnetic field	49
5.6	Magnetic field variation in the surrounding space of the magnetic dipole	50
5.7	Magnetic field variation as a function of the distance to the crack	51
5.8	Real and imaginary components of the complex susceptibility for the studied ferrofluid	53
5.9	Phase lag induced due to the presence of ferrofluid	54
5.10	Proposed method for measuring the phase lag induced due to the presence of ferrofluid inside the defect	54
C.1	USAF MIL-A-83444 safety requirements for assumed initial damage	67

C.2 Minimum detectable crack sizes for fracture analysis based on standard NDE methods	68
D.1 Custom-made solenoid blueprint	70
D.2 Trimetric view of the solenoid	70
D.3 Coil assembling	71
D.4 Sensor location within the support	71
D.5 Custom-made solenoid assembling	71
D.6 Semi-infinite solenoid with zero inner radius	72
D.7 Formation of a finite solenoid from four semi-infinite solenoids	73
D.8 Cross section of the solenoid's coil #1	75
D.9 Non-dimensional axial field of semi-infinite solenoid	75
D.10 Theoretical field obtained with coil #1 at the center of the solenoid	76
D.11 Series RL circuit diagram	76
D.12 Phase lag between the current and the input tension in a pure inductive circuit	77
D.13 Phase difference between the magnetic field signal and the input voltage	78
E.1 Scheme of the magnetic probe	79
E.2 Probe orientation for field measurement	80
E.3 Schematic of the probe polarity. Meter reads positive in this configuration	80
E.4 <i>Honeywell</i> HMC5883L axes orientation on <i>CRIUS MultiWii SE v0.2</i> board	81
E.5 Low-field magnetic flux density measured with <i>AlphaLab's</i> magnetometer and <i>Honeywell's</i> HMC5883L	82
E.6 Average of the low-field magnetic flux density data points measured with <i>AlphaLab's</i> magnetometer and <i>Honeywell's</i> HMC5883L	82

LIST OF TABLES

3.1	Examples of viscosity at 27° C	20
3.2	Examples of surface tension	21
4.1	Properties of the ferrofluid N-503 supplied by <i>Sigma Hi-Chemical Inc.</i>	37
4.2	Geometric characteristics of the costume-made solenoid	39
4.3	Summary of experimental conditions in DC tests	43
4.4	Summary of experimental conditions in AC tests	44
5.1	Geometric characteristics of the simulated crack and equivalent magnetic dipole	46
5.2	Ferrofluid magnetization	49
5.3	Maximum field variation at both the dipole's centre and the sensor position . . .	50
5.4	Parameters for the calculation of the AC magnetic susceptibility	53
A.1	Units for magnetic properties	63
B.1	Chemical composition in weight % of AA 2024-T3 and AA 7075-T6	65
B.2	Chemical composition in atom % of AA 2024-T3 and AA 7075-T6	65
B.3	Mechanical properties of AA 2024-T3 and AA 7075-T6	65
D.1	Parameters to obtain the contribution of each semi-infinite solenoid to the axial field	74
D.2	Necessary values to compute the total non-dimensional axial field	74
E.1	<i>AlphaLab, Inc.</i> High-Stability DC Magnetometer specifications	79

ABBREVIATIONS AND SYMBOLS

A list of abbreviations and the major symbols used to describe physical quantities, in the order in which they appear throughout the document, is presented.

Abbreviations

NDT	Non-Destructive Testing
DOC	Direct Operating Costs
AA	Aluminium Alloy
CFRP	Carbon Fibre Reinforced Polymer
GFRP	Glass Fibre Reinforced Polymer
MEDD	Magnetic Early Defect Detection
NED	Non-Destructive Evaluation
EASA	European Aviation Safety Agency
NMAB	National Materials Advisory Board
PCRT	Process Compensated Resonance Testing
ACFM	Alternating Current Field Measurement
CAGR	Compound Annual Growth Rate
DC	Direct Current
AC	Alternating Current

Symbols

Z	acoustic impedance
ρ_0	material density
c_0	speed of sound
ρ	density
m	mass, particle magnetic moment
V	volume, particle volume, electrical potential difference
SG	specific gravity
g	gravity constant
W	weight, energy of a magnetic dipole
Φ	ferrofluid volume fraction
η	carrier fluid dynamic viscosity
p	pressure
T	temperature
η_R	rotational viscosity
σ	surface tension
$M_{sat}^{material}$	bulk saturation magnetization
R	particle radius, distance from the magnetic dipole, resistance
D	particle diameter
M	magnetization
n	number of particles within a ferrofluid sample
M_d	domain magnetization

M_{sat}	ferrofluid saturation magnetization
μ_0	magnetic permeability of air
μ	magnetic permeability
B	magnetic flux density, induced magnetic field
H	magnetic field strength
χ	ferrofluid magnetic susceptibility
Ω	frequency of the input signal
χ_0	ferrofluid zero magnetic susceptibility
τ	characteristic time of the system
j	imaginary unit
χ'	real part (in-phase) of the complex susceptibility
χ''	imaginary part (out-of-phase) of the complex susceptibility
k_B	Boltzmann constant
Ω_{max}	frequency at which χ'' is maximum
$\tilde{\chi}'$	non-dimensional real part (in-phase) of the complex susceptibility
$\tilde{\chi}''$	non-dimensional imaginary part (out-of-phase) of the complex susceptibility
E_{th}	thermal energy
E_{VdW}	energy corresponding to the Van-der-Waals attraction
l	ratio of the distance between particles to the particle diameter
s	distance between particles, steric layer thickness, finite solenoid inner radius
D	particle diameter
A	Hamaker constant
E_{dd}	energy corresponding to the dipole-dipole interaction
d	particle magnetic diameter
E_{mag}	magnetic energy of a particle
E_g	potential energy of a particle in a gravitational field
$\Delta\rho$	difference in the densities of the magnetic material and the carrier fluid
h	height of the ferrofluid sample
T_c	Curie temperature
τ_B	Brownian relaxation time
τ_N	Néel relaxation time
f_0	Larmor frequency: frequency constant of the Néel relaxation
κ	anisotropy constant of the particle
τ_{eff}	effective characteristic time of the system
$\vec{\Gamma}$	torque exerted on a ferrofluid particle
\vec{H}	magnetic field vector
θ	zenithal angle between the particle magnetic moment and the applied magnetic field
H_0	magnitude of the external magnetic field
M_z	magnetization in the z -direction
\tilde{M}_z	non-dimensional magnetization in the z -direction
α	Langevin parameter, ratio of the solenoid's outer diameter to inner diameter
$\tilde{\Omega}$	non-dimensional frequency
\tilde{t}	non-dimensional time
$D_{r,max}$	rotational diffusion coefficient
L	length of the solenoid, inductance
I	current
r	distance from the wire, equivalent cylindrical dipole radius
ω	frequency of the input signal

a	semi-length of the crack and the cylindrical dipole
V_0	input tension
I_0	input current
H_z	magnetic field strength in the z -direction
\vec{B}	magnetic flux density vector
\vec{r}	position vector
∇	Nabla (or Del) operator
ϕ^*	scalar magnetostatic potential (a function of \vec{r})
ΔB_z	variation of the magnetic field in the z -direction due to the presence of ferrofluid
M_{AC}	ferrofluid magnetization under alternating current
H_{AC}	magnetic field strength produced by an alternating current
ϕ	phase lag of the ferrofluid magnetic signal relative to the magnetic drive signal, phase angle between the input tension and current
β	ratio of the solenoid's length to inner diameter
J	current density
b_i	radii of the semi-infinite solenoids ($i = 1, 2, 3, 4$)
h_i	non-dimensional fields of the semi-infinite solenoids ($i = 1, 2, 3, 4$)
h_z	axial non-dimensional field of the semi-infinite solenoids
Z_L	complex impedance of a RL circuit
X_L	reactance of the solenoid
f	frequency of the input signal

CHAPTER 1. INTRODUCTION

Since the beginning of the aerospace industry, safety has been one of the major concerns of aircraft designers and manufacturers to comply with the international regulations and satisfy the customers' requirements in this issue.

Around the 1950s, during the rapid growth of pressurized commercial flights, fatigue cracks caused several serious aircraft accidents. Probably the best known are those of the *de Havilland DH 106 Comet*, with three of them tearing apart during mid-flight in well-publicised accidents in 1953 and 1954. Fatigue can be defined as a form of failure due to a progressive and localized structural damage that occurs in structures subjected to dynamic and fluctuating loads. These circumstances make possible for failure to occur at stress levels clearly lower than the ultimate tensile stress or yield stress for structures subjected to static loads [1]. In this sense, fatigue is responsible for a major part of the failures of metal components and it can result in an unexpected and catastrophic failure. To address this problem, crack detection and monitoring became an issue of remarkable importance: aircraft manufacturers began the inspection of components before being assembled and maintenance providers periodically inspected them throughout their useful life. This fact introduced the Non-Destructive Testing (NDT) to the aerospace industry, which quickly became an indispensable tool for both production and maintenance.

Maintenance cost is probably the portion of the Direct Operating Costs¹ (DOC) where aircraft manufacturer has one of the greatest potential fields for improvement in reducing it. Aircraft maintenance cost, which includes routine maintenance as well as major overhauls for the airframe and engines, represents approximately 13 to 18% of a commercial aircraft's DOC [2], and may even reach 40% in some cases [3].

In light of these numbers, the success of the aerospace industry is doubtlessly dependent on NDT since the cost of maintaining and flying in airplanes would increase dramatically without it, while the safety of flying would decrease. Thereby, research on suitable NDT solutions for aerospace components that enhance safety and reduce derived costs certainly prove insightful to the aerospace and air transport industries, and ultimately the end users of their products.

The aim of this thesis was to assess the feasibility of an innovative NDT technique concept based on deposition of a ferrofluid consisting of magnetic nanoparticles in the test-piece surface. The proposed technique is applicable to inspection of any type of materials except to ferromagnetic materials. Thus, it is specially suited to detect surface defects in a wide range of materials typically used in aerospace applications, i.e. non-ferromagnetic materials like aluminum alloys (AA) or composite materials like Carbon Fibre Reinforced Polymer (CFRP) or Glass Fibre Reinforced Polymer (GFRP).

The proposed technique, which from now on will be referred to as Magnetic Early Defect Detection (MEDD), aims at meeting the requirements of NDT end-users in the form of a significant reduction of surface inspection costs, as compared with the most commonly used techniques at present day, aside from visual inspection.

¹The Direct Operating Costs of an aircraft include, among others, fuel, maintenance, crew and insurance.

After this introduction, the present thesis report is structured as follows:

Chapter 2 provides an overview of NDT with focus on the major techniques used nowadays as well as those recently emerging and the current worldwide equipment market estimates.

Chapter 3 is an introduction to magnetic fluids, describing its structure and providing several basic definitions and concepts to understand their properties. Besides, some theoretical models to describe their response to magnetic fields is presented.

Chapter 4 presents the NDT technique proposed in this thesis, by providing detailed information on the materials and tools which are necessary to reproduce the proposed technique and explaining the procedure to be followed to do so.

Chapter 5 shows the theoretical results obtained under different conditions for the proposed method and the discussion with regard to the results obtained in the experimental runs.

Finally, chapter 6 presents the result conclusions of this work and a proposal of future tasks to improve the obtained results provided that the project is to be continued.

CHAPTER 2. NON-DESTRUCTIVE TESTING

The chapter here presented gives an introduction to NDT with focus on the major techniques used nowadays and the current worldwide market estimates. Since giving a detailed description of NDT techniques is not the main objective of this document, references are provided throughout the text for further reading on the subject.

NDT has its origins prior to the 1920s, but development of the majority of methods that are known nowadays did not appear until late in the 1930s [4]. NDT can be defined as the inspection of a material or component, in search of defects, using a technique that does not risk inducing damage in its structure. This concept is extended, and known as Non-Destructive Evaluation (NDE), when combined with an assessment of the significance of any defects found. However, they are both terms often used interchangeably [5].

As it is described in EASA PART 145.A.45 (referred to maintenance data by manufacturers of aircraft, engine or propellers), NDT in aviation is the whole of tests performed for the purpose of sustaining the conformance of the aircraft or aircraft component in service. In a practical way, NDT is concerned with the performance of the test piece: how long may the piece be used and when it needs to be checked again.

Components used in the aerospace industry are designed to be as light as possible while still performing their intended function. This generally means that components carry very high loads relative to their material strength and small flaws can cause a component to fail. Since aircraft are subjected to cyclic loading as they fly, land, taxi, and pressurize the cabin, many components are prone to fatigue cracking after some length of time. Thereby, NDT plays a vital role in the production process, from a quality-assurance and cost-effective point of view, and in maintenance to prevent safety-critical components from failing.

2.1. Classification of NDT methods

NDT is divided into various methods, each of them based on a particular scientific principle, which can be completely characterized in terms of five principal factors [6]:

- Energy source or medium used to probe the test object.
- Nature of the signals, image or signature resulting from interaction with the test object.
- Means of detecting or sensing resulting signals.
- Method of indicating or recording signals.
- Basis for interpreting the results.

The National Materials Advisory Board (NMAB) classifies these methods into six major categories: visual and optical, magnetic-electrical, chemical-electrochemical, penetrating

radiation, mechanical vibration, and thermal [7]. A comprehensive description of the principles and application of the different methods can be found in the American Society of NDT Handbook [8]. These methods may be further subdivided into various techniques, the most used of which will be overviewed next.

The variety of techniques available can also be roughly broken down into two areas [9]: surface techniques, which are used to identify surface and near surface defects such as cracks and surface porosity, and sub-surface techniques, that can be used to detect defects that lie under the material's surface. Within the first group, most commonly used techniques are visual and optical testing, magnetic particle testing, liquid penetrant testing and electromagnetic testing. On the other hand, sub-surface techniques include radiography and ultrasonic testing among the most used.

2.1.1. Surface techniques

Visual and optical testing

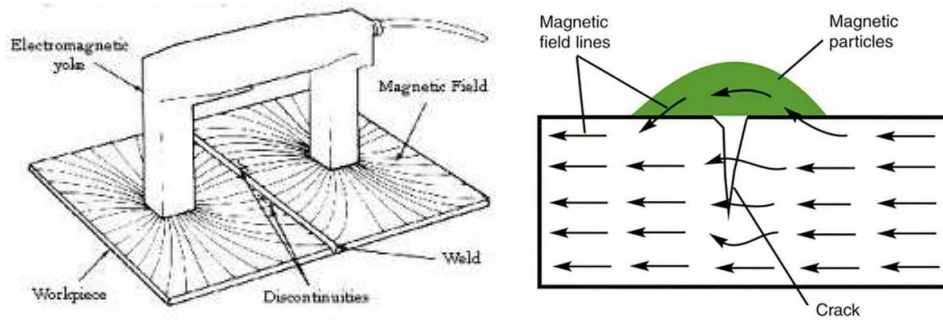
Over 80 percent of the inspections done to an aircraft are visual inspections, being often used as an initial screening method to detect gross defects and target subsequent testing by other methods. Visual examiners follow procedures that range from simply looking at a part to see if surface imperfections are visible, which requires proper training, to using computer controlled camera systems to automatically recognize and measure features of a component. Reference [10] provides further reading on visual and optical techniques.

Magnetic particle testing

Magnetic particle testing is specifically used for detecting flaws in ferromagnetic materials. The procedure consists in applying a magnetic field to the test object (Fig. 2.1(a)). Fine ferromagnetic particles (either dry or suspended in liquid) are then spread on the surface of the test object and their behavior is observed. If surface or near-surface discontinuities such as surface breaking cracks are present, the magnetic field is distorted and a "leakage field" that extends beyond the test object close to the flaw is produced, attracting the magnetic particles to the area so the anomaly can be detected (Fig. 2.1(b)). Although this technique reveals the location of the defects, it is often unable to determine its depth. Besides, it has the major drawback of requiring to magnetize (and frequently demagnetize) the component. Reference [3] provides a more detailed description of magnetic testing.

Liquid penetrant testing

Liquid penetrant testing is probably one of the most widely used NDT techniques. It is used for the detection of surface discontinuities in all metal and ceramic materials. This technique consists in applying a daylight visible penetrant solution which is drawn into small surface breaking defects of the pre-cleaned test object by capillary action. Following a



(a) Magnetic particle testing procedure. Source: Aerial Testing Company, Magnetic Particle Inspection
 (b) Accumulation of ferromagnetic particles around the flaw. Source: NDT Resource Center

Figure 2.1: Magnetic particle testing.

given time¹, ranging from 5 to 30 minutes depending on the material inspected, excess penetrant is removed from the surface and a developer in liquid or powder form is applied. This developer absorbs penetrant drawn from discontinuities and reveals a vivid color contrast between the penetrant and developer (usually red on white). Figure 2.2 illustrates the procedure. Fluorescent penetrants are also commonly used. In this case, an ultraviolet light is required for the defects to be revealed. This technique clearly relies on the operator to detect flaws so proper training is imperative. Liquid penetrant testing is covered in detail in reference [11].

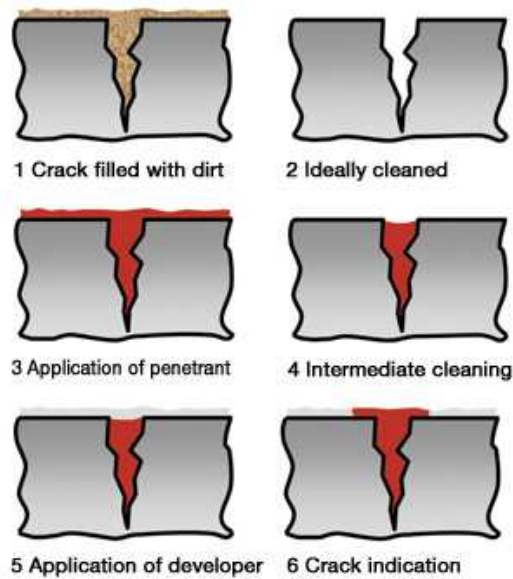


Figure 2.2: Liquid penetrant testing procedure. Source: Karl Deutsch, NDT Basic Knowledge: Penetrant Testing.

¹From now on called dwell or residence time.

Electromagnetic testing

Within the electromagnetic testing techniques, eddy current testing is perhaps one of the most versatile NDT techniques. Eddy current testing uses induced electrical currents to detect defects. Essentially, the technique uses a coil carrying an alternating current as transducer. This produces an alternating magnetic field parallel to the axis of the coil which in turn induces eddy currents in the surface of the test object. These eddy currents set up a magnetic field opposing that produced by the coil (Fig. 2.3), thus changing the impedance of the coil. Defects oriented normal to the surface of the test object cause interruptions in the flow of current, which changes the magnetic field and hence the coil impedance. Most eddy current testing is based on the measurement of the coil impedance, though it is possible to measure the magnetic field directly. Though, in general, the technique is used to inspect relatively small areas and is therefore better suited for inspecting areas where damage is already suspected, it nevertheless has a variety of applications: from measuring material thickness to detecting corrosion damage. As eddy currents are affected by the electrical conductivity of materials, they can also be used to sort materials and determine, for instance, whether a structure has been exposed to high temperatures. The disadvantages of this technique are that it is sensitive to lift-off, it is a point test, so scanning is required for large areas, and it is generally limited to near surface defect of conducting materials. Reference [12] provides further details on electromagnetic testing.

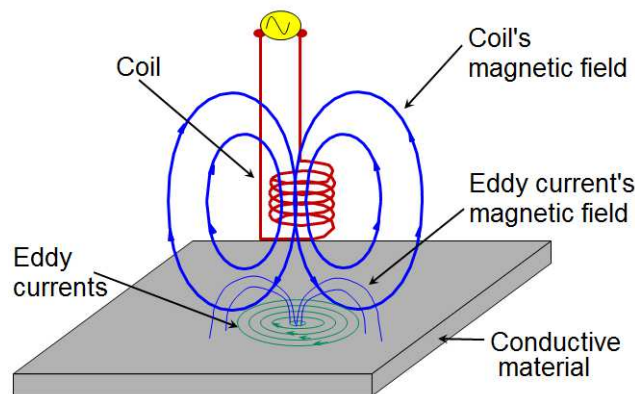


Figure 2.3: Eddy current testing procedure. Source: Collaboration for NDT Education, Introduction to Non-Destructive Testing.

2.1.2. Sub-surface techniques

Radiography testing

Radiography testing has its origins in the medical field. This technique consists in the use of gamma or X-rays to spot imperfections. Radiation is directed through the test object and, this way, any defect that reduces its absorption will result as a lighter area on a negative film (Fig. 2.4). Cracks are seen as a thickness variation and the larger the variation, the easier the crack is to detect. In this sense, when the path of the X-rays is not parallel to a crack, the thickness variation is less and the crack may not be visible (Fig. 2.5). This technique has a major disadvantage: the health hazard posed by radiation, which requires

expensive protective equipment and clearing the area when using on-site radiography with consequent disruption to operations. A more detailed description of radiography within NDT can be found in reference [13].

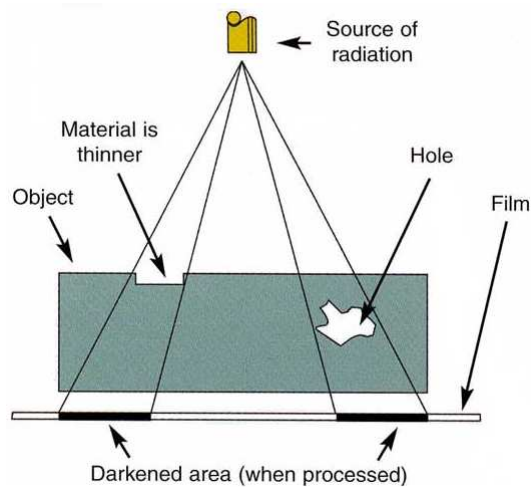


Figure 2.4: Radiography testing procedure. Source: NDT Resource Center.

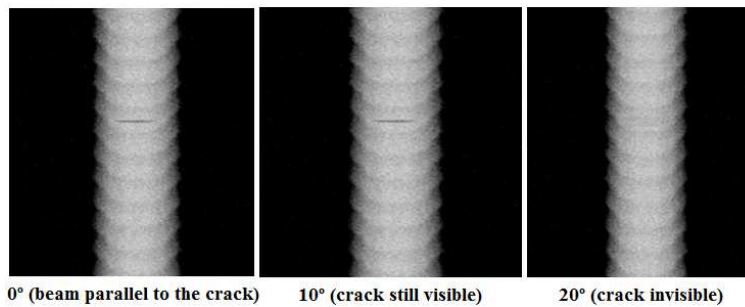


Figure 2.5: Sensitivity to crack orientation on radiography testing. Source: Collaboration for NDT Education, Radiographic Testing.

Ultrasonic testing

Ultrasonic testing, in its most commonly used form called pulse echo, is based on the introduction of high-frequency sound wave beams (normally ranging from 1-5 MHz) into the test object to detect sub-surface flaws. Defects are detected if they produce a change in the acoustic impedance² in the path of the ultrasonic beam. An open crack filled with air has very low acoustic impedance so it reflects virtually all the acoustic energy incident on it. Hence, the sound waves travel through the material and are reflected back from cracks or flaws. Since the speed of sound in the parent material is known, the reflected sound energy is then displayed versus time and analyzed to define the presence and location of flaws or discontinuities (Fig. 2.6). The major disadvantage of ultrasonic inspection is that it is essentially a point method, the area interrogated being limited to a region immediately surrounding the transducer. This means that scanning is required if large area is to

²The acoustic impedance indicates how much sound pressure is generated by the vibration of molecules of a particular acoustic medium at a given frequency and is given by the product of density and speed of sound, $Z = \rho_0 c_0$ [14].

be covered, which is time consuming and therefore expensive. Reference [15] provides further details of ultrasonic inspection.

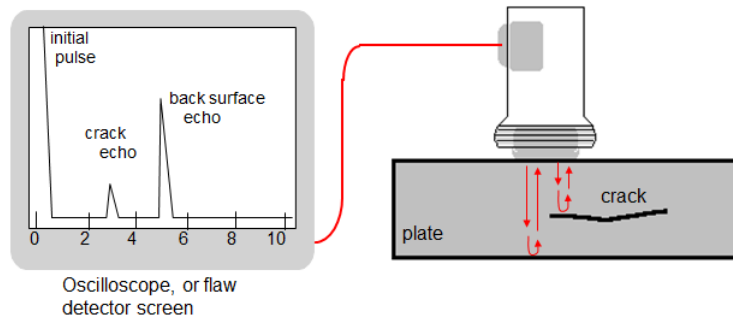


Figure 2.6: Ultrasonic testing procedure. Source: Collaboration for NDT Education, Introduction to Non-Destructive Testing.

2.2. Alternative and emerging techniques

Despite the techniques described in the previous section account for well over 90 per cent of the industrial NDT, there is a vast number of alternative methods such as thermography testing, process compensated resonance testing (PCRT), holography, shearography, alternating current field measurement (ACFM), and laser ultrasound. References on those techniques can be found in [5], whereas further description is reported in [16]. Some of these are still in development but with good chances to become part of the most commonly used NDT techniques. An overview of thermography testing and PCRT is provided in the following lines.

Thermography testing

Thermography testing is becoming more important every day in parallel to the development in composite technology. For instance, one technique showing increasing promise in the aerospace industry is pulsed thermography, in which infrared cameras can be used to detect sub-surface damage [9]. This technique, which is still being developed and holds particular promise for detecting flaws in sections of composite materials, consists in firing a rapid pulse of heat at the surface of the composite material and using an infrared camera to measure the temperature change over time. If there is a delamination within the test object it implies the presence of an air gap, which is more insulating and the temperature will not drop as quickly as in the rest of the test object. Further reading on the subject can be found in reference [17].

Process Compensated Resonance Testing (PCRT)

PCRT, which is based on resonant frequency response, is another emerging NDT technique which is showing great promise in the aerospace industry since it is said to detect

hidden flaws more effectively than other NDT processes do. The technology works by subjecting a part to a range of resonant frequencies and recording its response. Resonance frequencies are explicitly determined by the parts' elastic properties (stiffness), geometry and mass [18]. The presence of a structural defect changes the stiffness of the part and therefore changes the part's resonant frequencies. For a fixed geometry and mass, the change in frequency is proportional to the change in stiffness, and also to the severity of the defect. By comparing these results with known standard patterns, it is possible to identify defective parts in a manner that accounts for normal, acceptable part to part variation. A more detailed description of this technique and specific case studies from the aerospace industry, along with data demonstrating comparisons between traditional NDT and PCRT using real parts is presented in reference [19], whilst its application to manufacturing process control is reviewed in [20].

2.3. NDT method selection





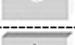



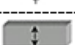
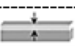
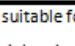
When selecting an NDT technique, the first issue to be addressed is the type and size of the defects that must be found. This is typically based on experience or, increasingly commonly, on fracture mechanics calculations. The range of techniques available and the cost of the inspection are critically dependent on this assessment since the choice of possible methods tends to reduce as the critical defect size reduces.

Each NDT method has its own set of advantages and disadvantages and, therefore, some are better suited than others for a particular application. For example, liquid penetrant testing, magnetic particle testing and eddy current testing are usually preferred for the investigation of fatigue discontinuities, whereas volumetric methods such as ultrasonic testing, radiography testing and thermography testing are preferred for the analysis of discontinuity entrapped within the structure. The table in Figure 2.7 provides some guidance in the selection of NDT methods for common flaw detection and measurement applications.

2.4. Global NDT equipment market estimates

This section is focused on exposing the key growth drivers, the current market trends and revenue forecasts and recent activity of the NDT industry. Major end-use markets for NDT equipment include automotive, aerospace, primary metals and foundry, petrochemical industries and transportation, among others.

It is worth mentioning that visual and optical techniques, which comprise most of the inspections, does not include the purchase of specific NDT equipment and thus are not addressed in market estimates.

Flaw type / Inspection method	Visual	Liquid penetrant	Magnetic particles (A)	Ultrasonic		Eddy current (B)	X-Ray
				Straight beam	Angle beam		
Surface breaking linear 	1	3	3	1	2	3	1
Surface breaking volumetric defect 	3	3	3	3	3	3	3
Near-surface linear & normal to surface 	0	0	2	1	2	3	1
Near-surface linear & parallel to surface 	0	0	0	3	3	0	0
Near-surface volumetric 	0	0	2	3	3	3	3
Subsurface linear & Normal to surface 	0	0	0	1	2	0	1
Subsurface linear & parallel to surface 	0	0	0	3	3	0	1
Subsurface volumetric 	0	0	0	3	3	0	3
Thickness measurement of thin materials 	0	0	0	3	3	3	3
Thickness measurement of thick materials 	0	0	0	3	3	0	3
Non-conductive coating thickness measurements 	0	0	0	2	2	3	1

*Surface refers to surface most suitable for the inspection given the various options

(A) Ferromagnetic materials only

(B) Conductive materials only

(0) Will not detect

(1) Not well suited

(2) Fairly well suited

(3) Ideal application

Figure 2.7: NDT method selection. Source: NDT Resource Center.

2.4.1. Drivers

With customers and manufacturers progressively concerned about the residual life of assets and production quality, interest in test solutions that identify defects and provide early warnings to avoid adverse consequences is on the rise. Over the years, this has resulted in improved market awareness, acceptance and implementation of NDT techniques. Besides, the integration of in-line process control measurements with NDT equipment, and deployment of NDT technology to characterize materials for rapid delivery of adequate data about failure modes, has considerably expanded the scope of NDT in recent years.

When referring to maintenance, NDT inspection service providers need to comply with customers' expectations by providing the best price and at the same time provide better services. The total expenditure on NDT is much higher than the numbers given by market estimates, since inspection in most industries requires intensive labor and additional expenses are derived depending on the applied technique. In this sense, reduction of inspection costs is probably the strongest driver for NDT equipment manufacturers to improve their products.

In addition to the stringent industry product specifications and tight quality control requirements set by the manufacturers, the increasing use of composite materials in the aerospace industry has been a spur to significant NDT research and development. Most composite inspection is nowadays done by ultrasonics. However, composites are often used for large areas of aerospace structures, so the need to scan makes conventional ultrasonic inspection very slow. Therefore, the challenge is to develop inspection techniques that can be applied in situ with a minimum of preparation.

Other growth drivers of the NDT inspection services market include the increasing adop-

tion of the technology in other industries such as electronics, energy and material testing, among other new upcoming markets.

2.4.2. Trends and revenue forecasts

Traditionally, North America and Europe have been the primary revenue contributors to the global NDT equipment market. However, in recent times growth has been driven primarily by the large developing countries in South America and Asia-Pacific. With regard to Asia-Pacific, India and China are the largest as well as the fastest growing regional markets for NDT equipment. In South America it is Brazil leading the growth with an increasing demand for NDT services, basically from the aerospace and power generation sectors. Finally, the rapid growth of infrastructure industry in Eastern Europe and Asia, and the general growth of transportation, power supply, oil and gas, and aerospace industries, increased the demand for frequent and quality inspection.

According to [21], the worldwide market was estimated to be \$960 million in the early 1990s, and its breakdown provided the aerospace sector with already more than 25% of the total world market over other industries (Fig. 2.8).

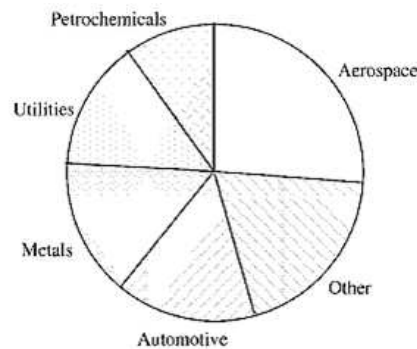


Figure 2.8: Estimated NDT market share by industry in the 1990s. Source: reference [21].

The global NDT market was not very much affected by the world economic crisis of 2008-09. There was indeed a decrease in the revenue growth rate, but it did not reach negative values. A key reason for this was a more stringent regulation, which compelled industries to perform inspections at specific intervals of time, and the already mentioned increase in NDT inspection demand from the Asian economies.

The expenditure on NDT equipment is nowadays estimated to be slightly more than \$1 billion and it is forecast to grow steadily and reach \$1.4 billion by 2017 [22]. Another recent market insight report [23] estimated the global market for NDT equipment to be \$1.1 billion in 2008 and experience a growth to \$1.3 billion by 2013, with expectations for it to grow at a CAGR³ of 3.2%.

³Compound Annual Growth Rate, often used to describe the growth over a period of time of some element of the business such as revenue, units delivered, registered users, etc.

2.4.3. Recent activity

A growing complexity of new materials and products is being introduced into the market for a wide range of applications in sectors such as aerospace and automotive sector. These materials will originate new products and drive the introduction of new testing techniques, especially of NDT. This way, ongoing research in material technology, the trend of miniaturization in the field of electronics, and the development of composite and other lightweight materials is likely to widen the scope of the NDT equipment and to lead to the outsourcing of testing services to third party providers with strong expert capabilities.

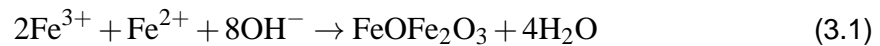
Within the NDT equipment industry, novel technologies and improvements in existing technologies are expected to provide better and faster testing. However, the NDT equipment is not allocated in large volume packages, being the size of the market relatively modest. But the fact that the product life cycle tends to be short implies the NDT companies supplying significant customer support to end-users, which should increase the revenue. The world NDT inspection services market is, though, highly fragmented with significantly high competition and so the financial performance of most NDT companies is rather poor [24]. As a matter of fact, the NDT equipment market is presently witnessing a spree of mergers, partnerships, and acquisitions among market players, which is resulting in a wide range of challenges and opportunities.

Due to the trend of consolidation of well established companies, smaller companies continue to face significant challenges in entering the NDT equipment market. The former exhibit superior capabilities in technological innovations, financial strength, global reach, service capabilities, and human capital. Factors influencing industry consolidation include increased competition, growing R&D costs, and the need to meet the demands of several end-use applications. This consolidation spree is likely to continue, and is expected to have a major effect on the NDT equipment market over the next few years.

CHAPTER 3. INTRODUCTION TO FERROFLUIDS

Magnetic fluids may be classified as *ferrofluids*, which are colloidal suspensions of very fine (*nm*-scale) surfacted magnetic particles, and *magnetorheological fluids*, which are suspensions of larger (*μm*-scale), usually non-stable, magnetic particles. These materials react differently to the application of an external magnetic field. Magnetorheological fluids undergo an enormous increase of viscosity and, for strong enough fields, they may even behave like a solid. Conversely, a ferrofluid keeps its fluidity even if subjected to strong magnetic fields ($\sim 10 \text{ kG}$) [25].

There are essentially two methods to produce ferrofluids, by size reduction and chemical precipitation. In size reduction, magnetic powder of micron size is mixed with the surfactant and the liquid carrier and grinded in a ball mill for a period of several weeks until the particles reach the desired nanometer-range size [26]. Chemical precipitation is a more efficient method to prepare magnetic nanoparticles, and probably the most used nowadays. Different procedures have been developed to achieve this goal. The necessary chemical reaction to precipitate the particles is given by [26]



Ferrofluids were initially synthesized in the 1960s and their applications did not stop to increase ever since then. Some examples of technological application include their use in heat dissipation and damping problems, dynamic sealing, lubricating and waste sorting. Besides, they also find application in biomedics, being used for magnetic drug targeting, clinical hyperthermia and magnetic separation of cells, among others [25, 27]. Most current applications employ static magnetic fields although the effects of alternating and rotating fields, which motivates much of the work discussed in this thesis, are being used to investigate future applications.

3.1. Structure of ferrofluids

Ferrofluids (also known as magnetic colloids) are liquid at room temperature. They are composed of magnetic particles modeled as a collection of single-domain, non-interacting dipoles, with typical dimensions of about 10 nm in diameter, dispersed in a liquid carrier which can be polar (water base) or non polar (oil) [28].

In order to avoid agglomeration due to the very short range Van-der-Waals attraction between the colloidal particles, they have to be coated with a shell of an appropriate material. According to the coating, the ferrofluids are classified into two main groups: *surfacted ferrofluids* if the coating is a surfactant molecule, and *ionic ferrofluids* if it is an electric shell. The ferrofluid used in this research is a commercial one of the first type, which's characteristics will be specified in Section 4.1.

3.1.1. Surfacted ferrofluids

In surfacted ferrofluids the particles are commonly magnetite (Fe_3O_4) coated with surfactant agents (such a stabilizing polymer) in order to prevent their aggregation. Steric repulsion¹ between particles acts as a barrier that keeps grains in the solution and stabilizes the colloid [30]. If the particles are dispersed in a nonpolar medium, as oil, one layer of the surfactant is needed to form an external hydrophobic layer. The polar head of the surfactant is attached to the surface of the particles and the carbonic chain is in contact with the fluid carrier (Fig. 3.1(a)). On the other hand, if the particles are dispersed in a polar medium, as water, a double surfactation of the particles is needed to form a hydrophilic layer around them (Fig. 3.1(b)).

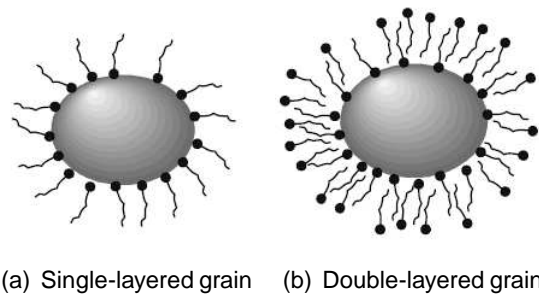


Figure 3.1: Sketch of surfacted ferrofluid grains. Source: reference [25].

3.1.2. Ionic ferrofluids

In ionic ferrofluids, the magnetic nanoparticles (usually maghemite, $\gamma\text{-Fe}_2\text{O}_3$, and different ferrites, $M\text{Fe}_2\text{O}_4$ ²) are electrically charged to keep the colloidal system stable [31]. An acid-alkaline reaction between particles and the bulk keeps their surface electrically charged [32]. Water is the usual liquid carrier and the pH of the solution can vary from about 2 to 12, depending on the sign of the surface charge of the particles. They can be positively charged, with $pH < 7$ (*acid ferrofluid*, Fig. 3.2(a)), or negatively charged, with $pH > 7$ (*alkaline ferrofluid*, Fig. 3.2(b)³).

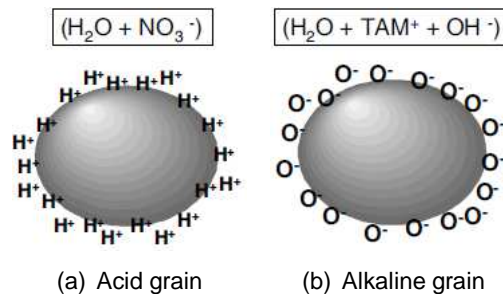


Figure 3.2: Sketch of ionic ferrofluid grains. Source: reference [25].

¹ Steric repulsion between particles occurs when a charged group on a molecule is spatially shielded by less charged (or oppositely charged) atoms [29].

² Where $M = \text{Mn, Co, Zn, Cu, Ni}$.

³ $\text{TAM}^+ \text{OH}^-$ is the tetramethylammonium hydroxide.

3.2. Ferrofluid properties

The aim of this section is to introduce and describe some terms in relation to the ferrofluid properties, some of which the author believes necessary to understand its behaviour under certain conditions, i.e. subjected to magnetization, the aim of the present research. The terms here presented are density, specific gravity, volume fraction, viscosity, pour point, surface tension, friction coefficient, coefficient of thermal expansion, magnetic moment, magnetization, saturation magnetization, magnetic permeability and magnetic susceptibility.

Density

Defined as usual as the ratio of mass of ferrofluid to its volume, $\rho = m/V$. If the volume of the ferrofluid is known, its mass can be calculated using the density value. Density increases with the saturation magnetization value of the ferrofluid.

Specific gravity

Specific gravity is the ratio of the density of a substance compared to the density (mass of the same unit volume) of a reference substance, usually water for liquids [33]. This way, those substances with a specific gravity greater than the unit are denser than water and viceversa. Specific gravity can be computed from different properties beside the densities ratio

$$SG = \frac{\rho_{sample}}{\rho_{H_2O}} = \frac{m_{sample}/V}{m_{H_2O}/V} = \frac{m_{sample}g}{m_{H_2O}g} = \frac{W_{sample}}{W_{H_2O}} \quad (3.2)$$

Volume fraction

The volume fraction of a ferrofluid, denoted by Φ , is the volume percentage of magnetic solid material with respect to the total volume including the carrier fluid and the surfactant [28]. Its value usually ranges from 5 to 15% for commercial distributions of dilute ferrofluids.

Viscosity

Viscosity, defined by η , is a measure of a fluid's resistance to flow, describing the internal friction of a moving fluid. A fluid with large viscosity resists motion because its molecular composition gives it a lot of internal friction. Conversely, a fluid with low viscosity flows easily because its molecular composition (generally small molecules with weak intermolecular forces) results in very little friction when it is in motion.

The ratio of the viscosity with the thermodynamic variables such as pressure p and temperature T is dependent on whether the fluid is Newtonian or Non-Newtonian.

Newtonian fluids. In this type of fluid an increase in p leads to a viscosity increase; besides, an increase in T leads to a reduction of the viscosity for liquids (owing to an extend of intermolecular distances), and an increase for gases (owing to the increase of molecular agitation). No functional relation $\eta = \eta(T, p)$ exists which is applicable to a wide variety of fluids.

Non-Newtonian fluids. In this type of fluid, the viscosity depends not only on the local thermodynamic variables p and T , but also in the shear rate.

In this sense, the behaviour of unmagnetized ferrofluids is Newtonian in nature (i.e., its viscosity is independent of the shear rate). This behaviour, though maintaining fluidity under strong magnetic fields, might become non-Newtonian under certain conditions such as dynamic magnetization. In this situation and depending on both the relative orientations and frequency of the external field and the particle's local vorticity, the particle rotation can be hindered (at low frequencies) or driven (at high frequencies) [34]. If the particle rotation is hindered, energy is dissipated via viscous friction between the particle and the carrier liquid, which leads to an apparent viscosity increase known as rotational viscosity η_R . On the other hand, if the particle rotation is driven this leads to an apparent decrease in fluid viscosity (the so called "negative viscosity") [35].

The viscosity of ferrofluids can vary from around 20 to 10000 centipose⁴.

Some examples of viscosity at a temperature of 27° C are listed in Table 3.1 below.

Table 3.1: Examples of viscosity at 27° C.

Substance	Viscosity η [cp]
Water	1
SAE 30 weight oil	500
SAE 40 weight oil	1000
Honey	12000

Pour point

The pour point is the temperature at which the ferrofluid becomes so viscous that it is unable to flow, but is not necessarily frozen. Ferrofluids are stable under freeze-thaw conditions.

⁴The centipose (cp) is the unit for dynamic viscosity in the CGS system, equal to 1 mPa · s in the SI system.

Surface tension

Surface tension σ is the property of a liquid arising from the imbalance of molecular forces at the surface. As a result, the free liquid surface is in tension and contracts as far as possible. It is due to this property that ferrofluids may exhibit capillary migration through narrow gaps, which is essential for the development of the technique object of research. The unit for its measurement is the dyn/cm.

Some examples of surface tension are listed in Table 3.2 below.

Table 3.2: Examples of surface tension.

Substance	Surface tension σ [dynes/cm]
Oil	32
Water	72
Mercury	513

Friction coefficient

Friction is the force that opposes sliding of one surface over the other, defined as the ratio of applied to normal forces on the moving piece. Friction is greatly reduced when a film of lubricant is present between two surfaces. Being ferrofluids normally synthesized from oils, with a friction coefficient of about 0.12, they possess excellent lubrication properties.

Coefficient of thermal expansion

The coefficient of thermal expansion is defined as the increment in volume of ferrofluid for a rise of temperature of 1° C. As an example of the order of magnitude, for an increase of temperature of 100° C, the initial volume of 1 ml of ferrofluid will grow to 1.06 ml, being sufficiently small to be neglected as an influencing property for the case of study.

Magnetic moment of a particle

The typical size of the magnetic particles of a ferrofluid is on the order of 10 nm including the surfactant material (which is around 2 nm thick). This makes the particles sufficiently small to be considered magnetic mono-domains, which is an important characteristic, because the particles have to have non-zero magnetic moments for the ferrofluid to show its magnetic properties [25].

Each particle in a ferrofluid has a permanent magnetic moment proportional to its volume V , in the form

$$m = VM_{sat}^{material} \quad (3.3)$$

Where $M_{sat}^{material}$ is the bulk saturation magnetization, which will be defined next. Being the particles modelled as spheres, their volume can be expressed as

$$V = \frac{4\pi}{3} R^3 = \frac{\pi}{6} D^3 \quad (3.4)$$

Introducing (3.4) into (3.3) we can rewrite the particle permanent magnetic moment expression by making the particle diameter D explicit

$$m = \frac{\pi}{6} D^3 M_{sat}^{material} \quad (3.5)$$

Magnetization

Magnetization is the vector field that expresses the density of permanent or induced magnetic dipole moments in a magnetic material. Net magnetization results from the response of a material to an external magnetic field, together with any unbalanced magnetic dipole moments that may be inherent in the material itself.

The magnetization M of a collection of n magnetic particles with magnetic dipole moment m dispersed in a volume V can be obtained from [36]:

$$M = \frac{1}{V} \sum_{i=1}^n m_i \quad (3.6)$$

And the result is given in A/m in SI units.

Saturation magnetization

The bulk saturation magnetization⁵ $M_{sat}^{material}$ (in literature also referred to as domain magnetization M_d) is a property possessed by soft and permanent magnetic materials. It is the maximum value of the magnetic moment per unit volume of the sample when all magnetic domains are aligned.

The saturation magnetization of the ferrofluid, M_{sat} , is given by the expression

$$M_{sat} = \Phi M_{sat}^{material} \quad (3.7)$$

where Φ is the previously described volume fraction.

The ferrofluid saturation magnetization can be expressed as M_{sat} if SI units (A/m) are preferred or $\mu_0 M_{sat}$ if Gaussian units (Gauss) are preferred. Conversions for this and other magnetic properties are listed in Appendix A.1.

⁵ $M_{sat}^{material}$ for magnetite is $4.84 \cdot 10^5$ A/m [27]

Magnetic permeability

The magnetic permeability is the ratio of magnetic flux density in a ferrofluid to the external magnetic field, in which the ferrofluid is present,

$$\mu = \frac{B}{H} \quad (3.8)$$

The value μ is a scalar if the medium is isotropic or a second rank tensor for an anisotropic medium. In general, permeability is not a constant, as it can vary with the position in the medium, the frequency of the field applied, humidity, temperature, and other parameters. In a nonlinear medium, the permeability can depend on the strength of the magnetic field [37].

Magnetic susceptibility

The magnetic susceptibility is a quantitative measure of the extent to which a material may be magnetized in relation to a given applied magnetic field. The magnetic susceptibility of a material, commonly symbolized by χ , is defined in the SI by the ratio of the magnetization within the material and the applied magnetic field strength, in the form

$$\chi = \frac{M}{H} \quad (3.9)$$

This ratio, strictly speaking, is the volume susceptibility, because magnetization essentially involves a certain measure of magnetism (dipole moment) per unit volume. A closely related parameter is the previously described permeability, which expresses the total magnetization of material and volume.

When the magnetic susceptibility is measured in response to an AC magnetic field (i.e., a magnetic field that varies sinusoidally), this is called AC susceptibility. AC susceptibility is a complex quantity, which is defined as follows according to the *Debye theory* [38]

$$\chi(\Omega) = \frac{\chi_0}{1 + j\Omega\tau} = \chi'(\Omega) - j\chi''(\Omega) \quad (3.10)$$

where

$$\chi_0 = \frac{M_{sat}\mu_0 m}{3k_B T} \quad (3.11)$$

and $\tau = 1/\Omega_{max}$ is the typical relaxation time for the system, being Ω_{max} the frequency at which (3.15) is maximum. The in-phase (real) and out-of-phase (imaginary) components of the complex susceptibility are thus given by

$$\chi'(\Omega) = \frac{\chi_0}{1 + (\Omega\tau)^2} \quad (3.12)$$

$$\chi''(\Omega) = \frac{\chi_0\Omega\tau}{1 + (\Omega\tau)^2} \quad (3.13)$$

Finally dividing by (3.11), the previous equations can be written in dimensionless form

$$\tilde{\chi}'(\Omega) = \frac{1}{1 + (\Omega\tau)^2} \quad (3.14)$$

$$\tilde{\chi}''(\Omega) = \frac{\Omega\tau}{1 + (\Omega\tau)^2} \quad (3.15)$$

$\tilde{\chi}'$ and $\tilde{\chi}''$ are presented in Figure 3.3. Note that $\tilde{\chi}''$ has a maximum at $\Omega\tau = 1$. By determining Ω (more precisely Ω_{max}) experimentally and assuming the monodispersity of the ferrofluid (i.e., particles with the same diameter) this model can lead to estimate the particle relaxation time (a concept which is further described in Section 3.4.2.) and subsequently the average particle diameter by isolation in (3.26).

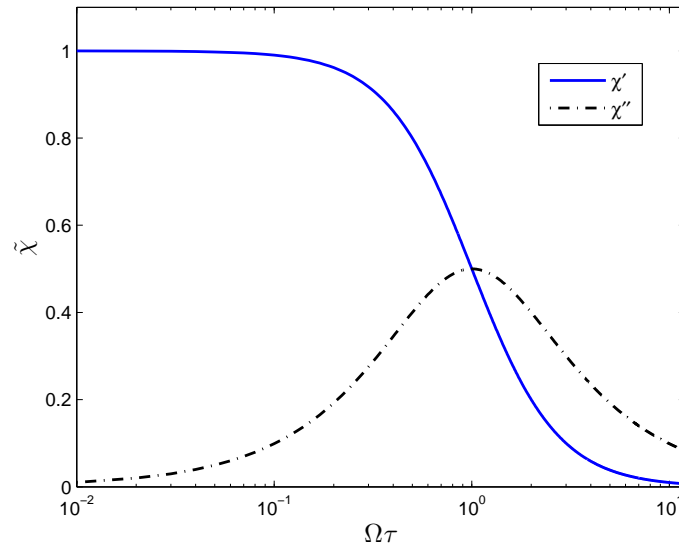


Figure 3.3: Real and imaginary components of the dimensionless complex susceptibility as a function of $\Omega\tau$.

3.3. Ferrofluid stability

The stability of magnetic colloids depends on the fine balance of six mechanisms [27] acting on the magnetic particles as attractive or repulsive interactions: Brownian motion⁶ (thermal energy), Van-der-Waals interaction, dipole-dipole interaction, elastic repulsion of the steric layers, separation in a magnetic field gradient and gravitational field.

In order to evaluate the stability of ferrofluids, the relative values of the energies corresponding to each mechanism have to be considered.

Brownian motion

The Brownian motion of the particles is a disordering mechanism and leads to the spontaneous redistribution of particles through the solution. This term can be expressed as thermal energy by the following expression

$$E_{th} = k_B T \quad (3.16)$$

being k_B the *Boltzmann's constant* and T the temperature in Kelvin.

Van-der-Waals interaction

This force between two spherical particles has its origin in the fluctuating dipole-dipole forces between them. The energy corresponding to the Van-der-Waals attraction can be expressed as [28]

$$E_{VdW} = -\frac{A}{6} \left[\frac{2}{l^2 + 4l} + \frac{2}{(l+2)^2} + \ln \frac{l^2 + 4l}{(l+2)^2} \right] \quad (3.17)$$

where $l = \frac{2s}{D}$, s is the distance between particles, D is the particle diameter and A is the *Hamaker constant*⁷.

Dipole-dipole interaction

The energy due to the dipole-dipole interaction considering two particles with aligned particles in contact can be defined as

⁶Rotational Brownian motion is the random change in the orientation of a polar molecule due to collisions with other molecules.

⁷The Hamaker constant is approximately 10^{-19} Nm for magnetite in solution [28].

$$E_{dd} = \left| -2 \frac{m_1 m_2}{4\pi\mu_0 V} \right| \quad (3.18)$$

where m is the magnetic moment of the particle, given by (3.3).

As for a ferrofluid to be stable, i.e., meaning the random disposition of particles in the solution is maintained, the energy due to the dipole-dipole interaction should be less or equal to the thermal energy given by (3.16), thus

$$E_{dd} \leq k_B T \quad (3.19)$$

Finally, being the magnetic moment of the particles dependent on the particle volume, according to [27] there is an expression for the maximum stable particle diameter (modelled as spheres) obtained from the combination of equations (3.3), (3.18) and (3.19),

$$D^3 \leq \frac{72k_B T}{\pi\mu_0 (M_{sat}^{material})^2} \leq k_B T \quad (3.20)$$

Elastic repulsion of the steric layers

The steric repulsion forces cause particles which approach each other in the range $\leq 2s \sim d/2$ (where s is the surfactant or steric layer thickness, and d is the particle's magnetic diameter) to be elastically repelled. Thereby, if the particles of a sterically stabilised ferrofluid collide, the stability of the dispersion is increased due to an elastic effect. This leads in turn to a further effective increase of the stable particle diameter.

Stability in a magnetic field gradient

The magnetic energy of a particle is given by

$$E_{mag} = \mu_0 m H \quad (3.21)$$

where m is again the magnetic moment of a given particle, expressed by (3.3).

As was previously stated, the magnetic energy of the particles should be smaller than that owing to thermal energy. Thus, considering the ratio of magnetic energy to thermal energy [28]

$$\frac{E_{mag}}{E_{th}} = \frac{\mu_0 m H}{k_B T} \leq 1 \quad (3.22)$$

and combining it with (3.3), the maximum stable particle volume (from which its diameter can be obtained if modelled as spheres) when this two energies are considered under certain conditions can be expressed as follows

$$V \leq \frac{k_B T}{\mu_0 M_{sat}^{material} H} \quad (3.23)$$

Stability in a gravitational field

In a similar way to that of the magnetic field gradient, the potential energy of the particles in a gravitational field can be expressed in a ratio to thermal energy, which again should comply with the condition of being smaller than the unity for the ferrofluid to be stable [28], thus

$$\frac{E_g}{E_{th}} = \frac{\Delta\rho V g h}{k_B T} \leq 1 \quad (3.24)$$

where $\Delta\rho$ is the difference in the material densities of the magnetic material and the carrier fluid⁸, g is the acceleration due to gravity and h is the height of the ferrofluid sample.

From (3.24), the maximum stable particle volume in a gravitational field can be isolated and expressed as

$$V \leq \frac{k_B T}{\Delta\rho g h} \quad (3.25)$$

3.4. Ferrofluid magnetization theory

When a paramagnetic⁹ or ferromagnetic material is stressed by a magnetic field, the magnetic dipoles within the material will attempt to align their magnetic dipole moment parallel to the direction of the applied field. The main difference between them is that whilst ferromagnetic materials display a strong magnetic interaction between neighboring molecules, paramagnetic materials display only weak interactions.

Thereby, when the suspension is exposed to an external magnetic field, the magnetic dipole moments of the particles tend to align with the field [36] and the material is thus described as being magnetized, meaning that it produces a net magnetic field in addition

⁸Typically, for a ferrofluid made of magnetite particles in a non-polar medium, $\rho_{magnetite} = 5046 \text{ kg/m}^3$ and $\rho_{hydrocarbonoil} \simeq 900 \text{ kg/m}^3$, giving a $\Delta\rho \simeq 4150 \text{ kg/m}^3$.

⁹Paramagnetism is the property whereby a material shows magnetic alignment in the presence of an external magnetic field, but has no (long-range) magnetic ordering in its absence. Materials which typically exhibit paramagnetism are liquid oxygen, rare-earth salt solutions and ferromagnets above the Curie temperature T_C , being the latter the temperature where a material's permanent magnetism changes to induced magnetism, or vice versa [39].

to the applied external magnetic field. Sensing this variation in the magnetic field is the main goal of the technique presented in Chapter 4.

3.4.1. Particle models

The particles within a ferrofluid are usually modelled as tri-axial ellipsoids, with physical and magnetic properties written in a Cartesian coordinate system with axes aligned with the principal axes of the ellipsoid rather than relative to the coordinate axes of the laboratory space [36]. An ellipsoid has three principal axes a_1 , a_2 and a_3 , directed along the x' , y' and z' -axis, respectively. The particles can thus be modelled as spherical particles $a_1 = a_2 = a_3$ (Fig. 3.4(a)); prolate ellipsoids ($a_1 = a_2 < a_3$) (Fig. 3.4(b)); oblate ellipsoids $a_1 < (a_2 = a_3)$; and scalene ellipsoids $a_1 \neq a_2 \neq a_3$.

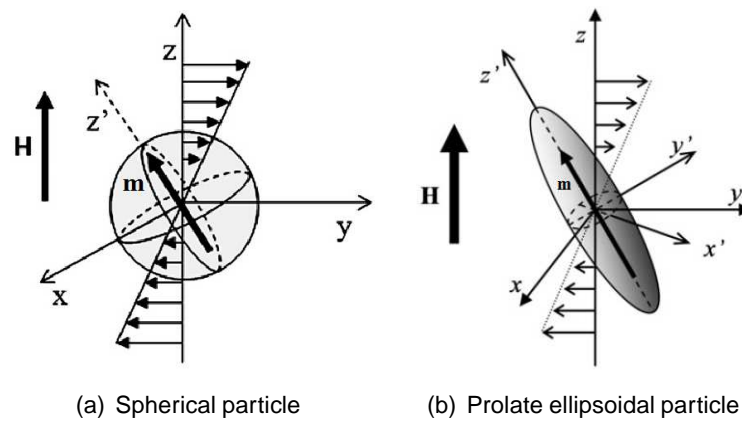


Figure 3.4: Particle models and system of coordinates. Source: Fig. 3.4(a) [40], Fig. 3.4(b) [41].

Note in Figure 3.4 that the magnetic dipole moment of the particle m is considered directed along one of the principal axes of the ellipsoid, and the external magnetic field H is assumed to be applied along the z -axis direction.

3.4.2. Magnetic relaxation theory

This section is concerned with the mechanisms of rotation of the dipole magnetic moments when subjected to an external magnetic field. Two dominant mechanisms exist through which the magnetic moments of the ferrofluid particles may align with the applied magnetic field: the *Brownian relaxation* (or *Debye relaxation*), which involves the physical rotation of the particle into alignment with the field, and the *Néel relaxation*, which is characterized by the movement of the particle magnetic moment relative to its crystal axis. Both mechanisms are sketched in Figure 3.5, where the ferrofluid particles are presented as non-spherical in order to facilitate the visualization of the relaxation process.

Each mechanism has a relaxation time for the magnetic moment rotation when subjected to a magnetic field, which for spherical particles can be written as stated in [28] for the Brownian relaxation time

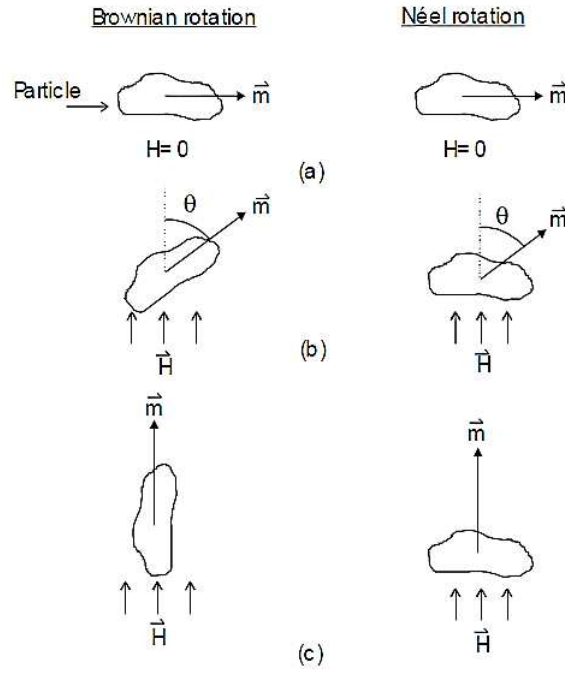


Figure 3.5: Brownian relaxation compared to Néel relaxation. Source: reference [42].

$$\tau_B = \frac{3V\eta}{k_B T} \quad (3.26)$$

where η is the carrier fluid dynamic viscosity.

And the Néel relaxation time, which is strongly dependent on the particle's volume and on the temperature,

$$\tau_N = \frac{1}{f_0} e^{\frac{\kappa V}{k_B T}} \quad (3.27)$$

being V the particle volume (considered spherical and given by (3.4), f_0 is the frequency constant of the Néel relaxation known as the *Larmor frequency*¹⁰, and κ is the anisotropy¹¹ constant of the particle.

The relaxation times defined in (3.26) and (3.27) are typically on the order of 10^{-5} to 10^{-9} seconds [28].

Finally, the effective relaxation time of the ferrofluid particles can be obtained by considering that the above mentioned processes act simultaneously. The characteristic time can then be written as a combination of both in the following form

$$\tau_{eff} = \frac{\tau_B \tau_N}{\tau_B + \tau_N} \quad (3.28)$$

¹⁰Typically on the order of $10^9 - 10^{10}$ Hz for magnetite [43].

¹¹Magnetic anisotropy refers to the crystallographic anisotropy of the particles and their divergence from the ideal sphere topology. In the case of magnetite, $\kappa = 1.1 \cdot 10^4$ J/m³ [44].

Between the Brownian and Néel relaxation, the one that has the smallest time constant dominates the physical process of relaxation. Regarding this fact and assuming polydispersity, for small particles within the ferrofluid it is the Néel time constant that dominates in (3.28) whereas it is the Brownian time constant for large particles.

3.4.3. Equilibrium (DC) magnetization

The magnetization of a material as a function of the external magnetic field can be represented in a magnetization curve, obtained from what is known as the *Langevin* relation for paramagnetic behaviour. This equation is derived from the assumption that ferrofluids consist of a collection of individual, non-interacting and monodisperse¹² magnetic dipoles. It is beyond the scope of this thesis to derive the governing equation of ferrofluid magnetization and the reader can refer to references [27] and [42] for an extensive description, but the model will be roughly introduced in the following lines.

The Langevin model is obtained from the equations defining the torque $\vec{\Gamma}$ and the energy W of a magnetic dipole with a certain magnetic moment \vec{m} and at a certain angle θ to a magnetic field $\vec{H} = H_0\hat{z}$ [28, 45]. The torque experienced by a particle in the ferrofluid is defined as

$$\vec{\Gamma} = \mu_0 \vec{m} \times \vec{H} = \mu_0 m H \sin \theta \quad (3.29)$$

And the particle energy is equal to the mechanical work required to rotate the particle through the angle θ

$$W = \int_0^\theta \Gamma d\theta = -m\mu_0 H [\cos \theta - 1] \quad (3.30)$$

Note in (3.30) that the energy is null at $\theta = 0$ (parallel to the field), it is $\mu_0 m H$ at $\theta = \pi/2$ (normal to the field) and has its maximum of $2\mu_0 m H$ at $\theta = \pi$ (antiparallel to the field).

Although the dipole magnetic moment tends to align itself with the field, there is an additional thermal energy (previously introduced in Section 3.3. as Brownian motion) which counteracts this behaviour and provides a randomizing spatial orientation. From thermodynamics, the situation can be described using Boltzmann statistics, introducing the number density of dipoles of a sample, in the form

$$n = \hat{n} e^{-W/k_B T} \quad (3.31)$$

One final equation is needed to obtain the final form of the Langevin equation. The net magnetization of the ferrofluid will be parallel to the direction of the applied magnetic field (Fig. 3.6). In this study we are concerned with the magnetization in the direction of the

¹²This means the whole set of particles have the same diameter.

applied field. Being the latter applied in the z -direction, the differential expression for the magnetization over a spherical volume containing a certain number of dipoles is

$$dM_z = \frac{nm}{V} \cos \theta r^2 \sin \theta dr d\theta d\varphi \quad (3.32)$$

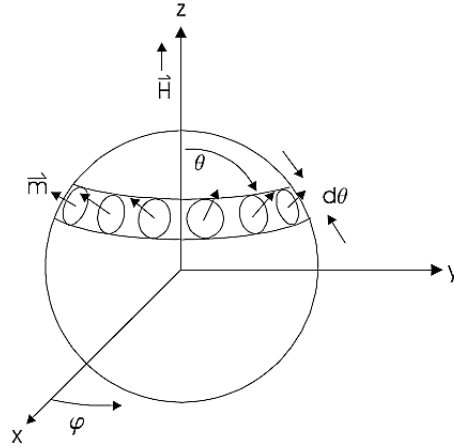


Figure 3.6: Contribution of the dipoles within a sphere to the net magnetization of a body. Source: reference [42].

Introducing (3.30) into (3.31) and substituting the latter into (3.32) yields an expression which can be integrated over the volume of the sphere and results in the Langevin function for paramagnetic behaviour

$$\tilde{M}_z = \frac{M}{M_{sat}} = \mathcal{L}(\alpha) = \coth(\alpha) - \frac{1}{\alpha} \quad (3.33)$$

where α is the so-called *Langevin parameter* defined as

$$\alpha = \frac{m\mu_0 H}{k_B T} = \frac{\pi}{6} \frac{\mu_0 M_{sat}^{material} H D^3}{k_B T} \quad (3.34)$$

If the ferrofluid is subjected to a steady DC magnetic field, its particles will eventually achieve an equilibrium state and the magnetization is described by the above stated equation (3.33). Figure 3.7 shows the dimensionless magnetization as a function of the Langevin parameter. Simulations provided in literature show that this result is applicable in DC magnetization regardless of the particle shape. This is to be expected because the energy necessary to rotate the particle into the field direction is a function only of the zenithal angle θ of the particle magnetic moment relative to the applied field direction [36].

The high-field region in Figure 3.7 is also known as the saturation region because it describes the approach to a saturation value of magnetization, point at which most of the dipoles have aligned with the magnetic field.

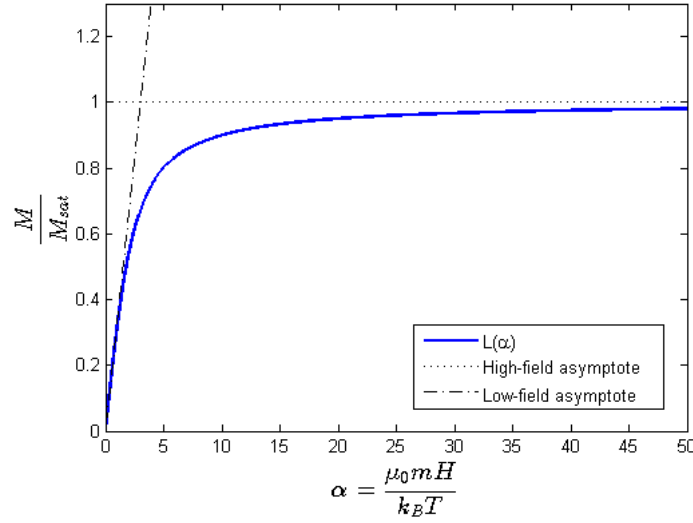


Figure 3.7: Dimensionless equilibrium magnetization as a function of Langevin parameter.

3.4.4. Dynamic (AC) magnetization

The behaviour of ferrofluids in AC magnetic fields can be vastly different than in DC fields because there exists a certain phase lag between the magnetization of the ferrofluid particles and the applied magnetic field, so that unlike the DC case the magnetization is not collinear with the applied magnetic field. This non-alignment of the magnetic field and magnetic moment results in a body torque on the ferrofluid. Physically, the ferrofluid particles individually experience a magnetic torque as was introduced previously in (3.29), given by the cross product of the particle's permanent magnetization and the time-varying magnetic field, that is

$$\vec{\Gamma} = \mu_0 \vec{m} \times \vec{H}$$

where \vec{H} is now an AC produced magnetic field which can be defined as

$$\vec{H} = H_0 \cos(\Omega t) \hat{z} \quad (3.35)$$

The ensuing dynamics are dependent upon the speed with which the particles can rotate into alignment with the field, known as the magnetic relaxation characteristic (Section 3.4.2.), and the frequency of the applied magnetic field. This way, with an external oscillating magnetic field, the dipole moment of the particles will follow the oscillations of the magnetic field with a certain phase lag which may be detected by appropriate means. Analogously to what was done in the previous section, the magnetization in which we are interested is that in the z -direction, thus

$$\tilde{M}_z = \frac{1}{3} \alpha \left[\tilde{\chi}' \cos(\Omega t) + \tilde{\chi}'' \sin(\Omega t) \right] \quad (3.36)$$

In the above stated equation, $\tilde{\chi}'$ and $\tilde{\chi}''$ are the non-dimensional real part (in-phase) and imaginary part (out-of-phase) of the *complex susceptibility* defined previously in (3.14) and (3.15), respectively. Various phenomena (such as resonances) can be seen in AC susceptibility that cannot be seen in constant-field (DC) susceptibility and this is an interesting feature to be exploited.

Simulations found in [36] show that particle shape (Section 3.4.1.) can slightly influence the ferrofluid magnetization in alternating magnetic fields by means of an increase of the particle relaxation times which introduces a certain lag with respect to the ideal spherical particle magnetization (Fig. 3.8). Throughout this thesis, though, the particles will be considered spherical, since the effects of particle shape can be neglected in most of the magnetization processes.

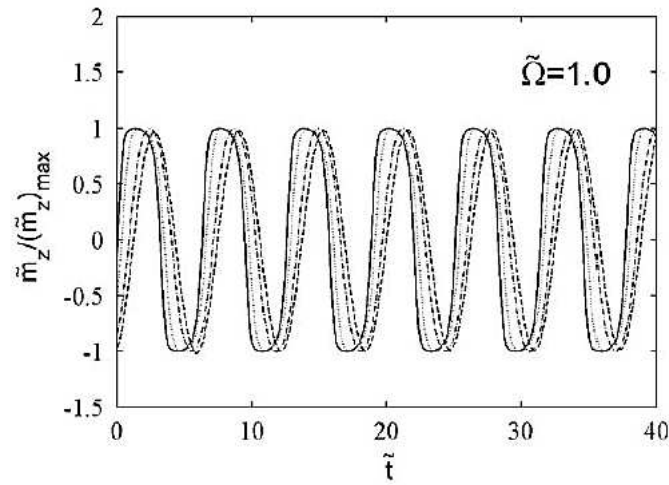


Figure 3.8: AC magnetization of suspensions of ellipsoidal particles for $\alpha = 10$ and $\tilde{\Omega} = 1.0$. $\tilde{\Omega}$ and \tilde{t} are the non-dimensional frequency and time given by $\tilde{\Omega} = \Omega/D_{r,max}$ and $\tilde{t} = t D_{r,max}$, respectively. $D_{r,max}$ is the *rotational diffusion coefficient*. Legend: (-) spheres, (- -) prolates, (- · -) scalene-1, (· · ·) scalene-2, (· · ·) oblates (indistinguishable from spheres). Source: reference [36].

CHAPTER 4. MAGNETIC EARLY DEFECT DETECTION

This chapter is aimed at introducing the proposed NDT technique object of this research, called Magnetic Early Defect Detection (from now on MEDD).

In light of what stated in the previous chapter, current research interest on ferrofluids is driven in part by the many phenomena ferrofluids display when exposed to various direct current (DC) and alternating current (AC) produced magnetic fields. In spite of this scientific interest, there remains a lack of extensive research and application of ferrofluids in situations where they are exposed to external alternating magnetic fields. Their rich behaviour in time-varying magnetic fields yet suggests potential applications in this direction.

The proposed NDT method seeks to exploit the above mentioned concepts of ferrofluid magnetization, previously described in Sections 3.4.3. and 3.4.4. In particular, MEDD method consists in the following procedure:

1. The surface to be inspected is initially scanned with a transducer capable of sensing the local value of magnetic flux density.
2. A suitable magnetic fluid, such as a custom-made suspension or commercially available ferrofluid with known magnetic properties, is then spread on the surface to be inspected.
3. The magnetic fluid is allowed to seep into any existing surface-breaking defect by capillary action for a given dwell time. This causes the accumulation of magnetic particles inside the defects, which may generate a detectable magnetic signal when magnetized.
4. The surface is then to be scanned again with a transducer capable of sensing the local value of magnetic flux density. This should enable a simple and rapid detection of surface-breaking defects thanks to the anomalous magnetic signals generated by the aggregated magnetic particles inside them.

Particularly, the proposed technique would be applicable for surface inspection of materials not necessarily magnetic or conductive, and of course aluminium alloys (AA) and composites like Carbon Fibre Reinforced Polymer (CFRP) or Glass Fibre Reinforced Polymer (GFRP). Composites are becoming increasingly important to the air transport industry since the 1980s, and detection of defects in these materials is nowadays one of the most attractive challenges to the NDT industry, as the most common NDT techniques are not generally suitable. Eddy current and magnetic particles testing are only applicable to conductive and magnetic materials, respectively. Liquid penetrant, ultrasonic and radiographic testing are troublesome and do not allow fast inspections. Finally, General Visual Inspection (GVI) is highly operator-dependent and presents significant limitations as per the dimensions of the detectable defects.

4.1. Experimental set

The experimental set here presented is not the design of the author but of his supervisor, Dr. J.I. Rojas. His directions and technical advice are acknowledged.

According to what exposed at the beginning of this chapter, two methods are envisioned considering the source with which the magnetic field is generated to magnetize the ferrofluid, i.e. DC source and AC source. The materials and instrumentation necessary to reproduce the method for both cases are defined in the following lines.

Direct Current (DC) tests: a precision pipette, (1) a commercial ferrofluid, (2) a test specimen, (3) a commercial magnetometer, (4) a custom-made solenoid, (5) a commercial multimeter, (6) a commercial power supply and (7) connection cables. The numbered components are shown in Figure 4.1(a).

Alternating Current (AC) tests: a precision pipette, (1) a commercial ferrofluid, (2) a test specimen, (3) a commercial magnetometer, (4) a custom-made solenoid, (5) a commercial function generator, (6) a commercial oscilloscope and (7) connection cables. The numbered components are shown in Figure 4.1(b).

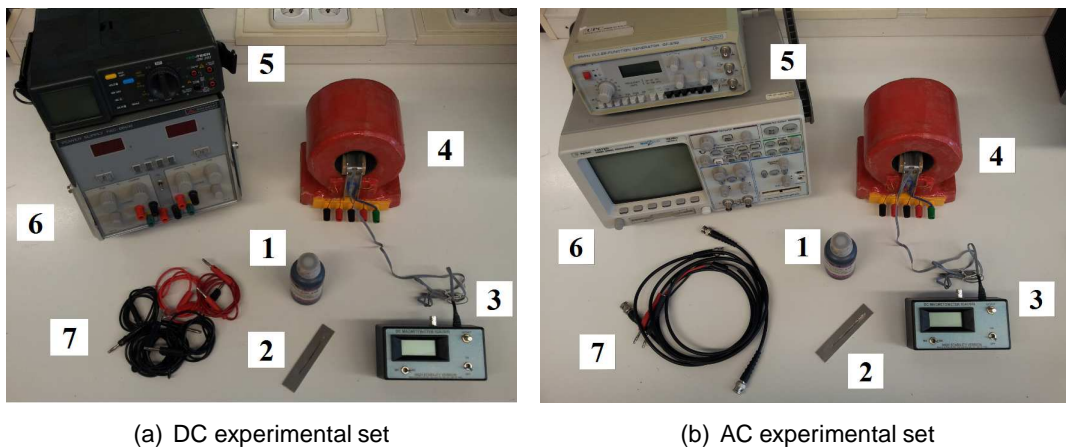


Figure 4.1: MEDD experimental set.

4.1.1. Magnetic fluid

The test ferrofluid was the type N-503 supplied by *Sigma Hi-Chemical Inc.* The properties of this magnetic fluid are summarized in Table 4.1, as provided by the manufacturer.

4.1.2. Test specimen

The tests were performed on a cracked sample of DURAL (SAE 2024-T3). This AA, along with ERGAL (SAE 7075-T6), is widely used in aircraft skin panels, especially in military

Table 4.1: Properties of the ferrofluid N-503 supplied by *Sigma Hi-Chemical Inc.*

Characteristic	Symbol	Value
Magnetic particles		Magnetite (Fe ₃ O ₄)
Carrier fluid		Iso-paraffin
Boiling range		150-200° C
Volume fraction	Φ	8.9%
Average diameter	D	10 nm
Specific gravity	SG	1.38 (at 20° C)
Dynamic viscosity	η	20.6 mPa · s
Surface tension	σ	29 dyn/cm
Saturation magnetization	M_{sat}	531 G (53.1 mT)

aircraft [46, 47], but also in commercial civil aviation aircraft [48]. The mechanical properties and chemical composition of these AA is presented in Appendix B.

The test specimen was machine cut from sheet of as-received AA 2024-T3, as a rectangular plate of 100 mm in length, 20 mm in width and 1.5 mm in thickness. The latter was selected in accordance with typical orders of magnitude for thickness of AA skin panels in aircraft, i.e. 1.0-1.6 mm for plain panels without holes and 2.0-3.0 mm for critical (heavy loaded) panels like those in the wing, the Horizontal Tail Plane (HTP) and the Vertical Tail Plane (VTP).

Selection of the dimensions of the studied crack

In aircraft structural design, for meeting fail-safe and damage tolerance requirements, the initial crack depends on the component and the type of flaw evaluated. For surface flaws, the pre-service inspection with high standard NDE assumes an initial damage of 1.27 mm for fail-safe (3.18 mm for slow-flaw growth), whereas it is assumed of 6.35 mm for in-service inspection. Appendix C shows a table that summarizes data with regard to this and other types of initial flaws. The same appendix shows a table summarizing the size of the minimum detectable cracks with the standard NDE methods except GVI [49]. In structural applications of AA panels in aircraft, e.g. fuselage skin, the most widely used NDT method is GVI. For instance, visual inspections with intervals of 6000-7000 flights (approximately once per year) are regarded as the main means for crack monitoring in Russia [50]. For the latter, the length of the detectable crack is assumed between .2 and .5 inches (5.08 and 12.70 mm).

A preliminary series of analytical results showed that the magnetic field induced by the ferrofluid was very weak for these target crack dimensions to be detected by the available instrumentation. Notwithstanding this fact, the research had still great scientific interest and a crack of larger dimensions was used in this study. In particular, a crack of 63 mm long, 1.5 mm wide and 0.5 mm deep was simulated¹ along the sample longitudinal symmetry axis by using a metal saw (Fig. 4.2).

¹As stated in the Federal Aviation Administration (FAA) 1998 Advisory Circular (AC)-25.571-1C Damage Tolerance, simulated cracks can be used in fatigue investigations instead of real cracks grown by fatigue during operation or dynamic testing [51].



Figure 4.2: Test specimen with simulated crack.

4.1.3. Custom-made solenoid

A multilayered solenoid² was conceived to be used as an electromagnet during the tests. This way, a radially thick solenoid with rectangular cross section was obtained by winding the wire back and forth and thus making several layers as shown in Figure 4.3.

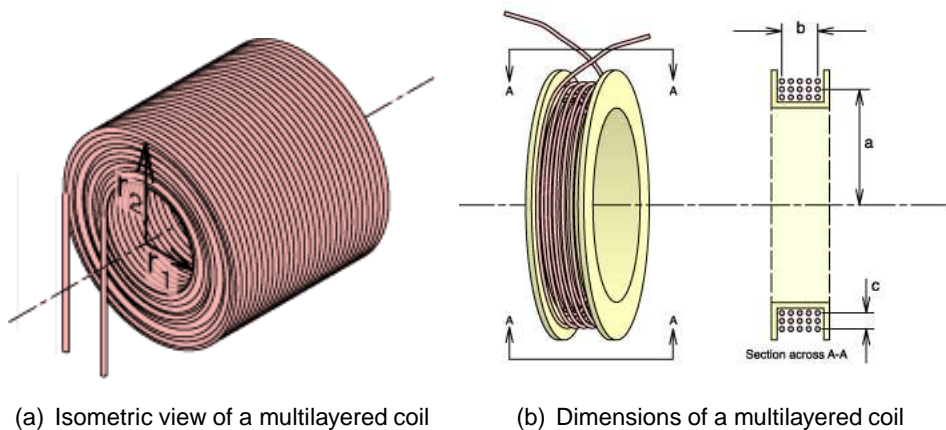


Figure 4.3: Example of a radially thick, multilayered solenoid with rectangular cross section.

The solenoid basically consists of two concentric copper wire coils (#1 and #2) covered by an external plasticine shell. The coils can be fed independently or can be connected in series or in parallel. A bracket for the test specimen was placed in the middle of the solenoid air gap, in a way such that the sample and the crack in its surface are aligned with the revolution axes of both coils. Figure 4.4 shows a design of the solenoid and the mentioned bracket for the test specimen, done with a commercial CAD software. Appendix D presents further details on both the solenoid design and construction process.

Table 4.2 summarizes the geometrical characteristics of the inner and outer coils comprising the solenoid used in the experiments.

As stated by magnetism theory, a current through a wire produces a magnetic field oriented according to the right-hand rule (Fig. 4.5). The field due to current flowing in a long straight

²A solenoid is a coil wound into a tightly packed helix which produces a uniform magnetic field in a volume of space (where some experiment might be carried out) when an electric current is passed through it [52].

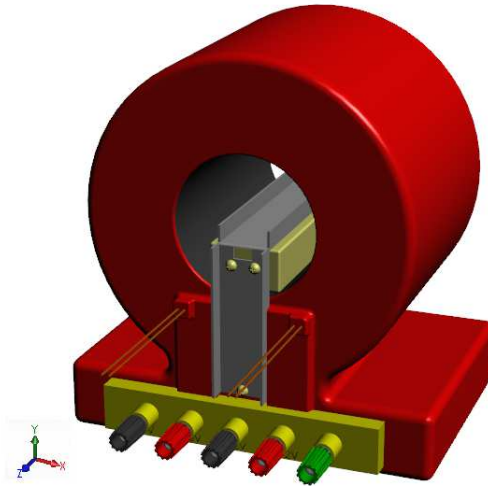


Figure 4.4: CAD of the custom-made solenoid.

Table 4.2: Geometric characteristics of the costume-made solenoid.

Coil #1		
Characteristic	Symbol	Value
Length	L	100 mm
Inner radius	r_1	30 mm
Outer radius	r_2	40 mm
Coil #2		
Characteristic	Symbol	Value
Length	L	100 mm
Inner radius	r_3	40 mm
Outer radius	r_4	68 mm

wire is always perpendicular to the wire and decreases as the inverse first power of the distance from the wire,

$$B = \frac{\mu_0 I}{2\pi r} \quad (4.1)$$

The net result is a field that goes in circles. The lines of force are circles concentric with the wire and the field is the same all the way around each circle.

With that said, if the wire is bent around into a loop, the current flowing through it produces what is known as a *dipole field* (Figure 4.6). This way the magnetic field produced by a solenoid is much like that of a bar magnet and can be obtained by summing the magnetic field generated by each separate wire winding.

In an ideal case as it is an infinitely long solenoid, the inner magnetic field is homogeneous and its strength does not depend on the distance from the axis, nor on the solenoid cross-sectional area. In reality, the magnetic field inside a finite solenoid varies both radially and longitudinally along its revolution axis. With the intention to measure the magnetic

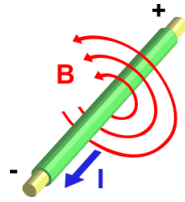


Figure 4.5: Magnetic field produced by a wire with an electric current through it. The field is oriented according to the right-hand rule. Source: reference [53].

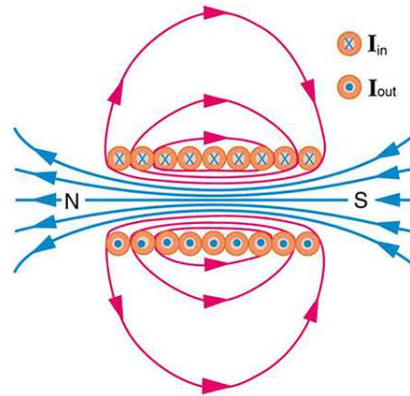


Figure 4.6: Magnetic field produced by a solenoid.

field variation at the center of the solenoid's air gap, where the magnetic field is maximum (Fig. 4.7), let us assume that it is radially uniform and it does not experience longitudinal variations.

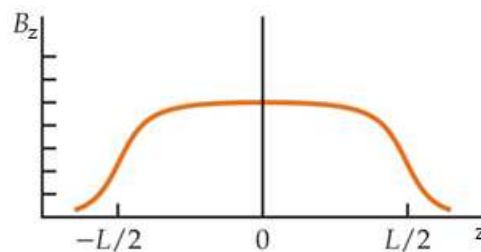


Figure 4.7: Magnetic field distribution along the solenoid revolution axis. L is the length of the solenoid.

Due to the multilayer winding characteristics, the DC magnetic field produced inside this custom-made solenoid can not be computed by means of the classical expression for a single layer solenoid with no core given by

$$B = \mu_0 \frac{NI}{L} \quad (4.2)$$

Instead, a more complex model based on tabulated data has been found in the literature. This model is reviewed in Appendix D, and Figure 4.8 shows both theoretical and experimental results of the magnetic field produced by the coil #1, which for simplicity is the one that has been considered during the realization of this thesis. The average error

obtained between theoretical calculations and actual measured values of the DC magnetic field was around 3%. Therefore, it can be concluded that the model is consistent with the experimental results

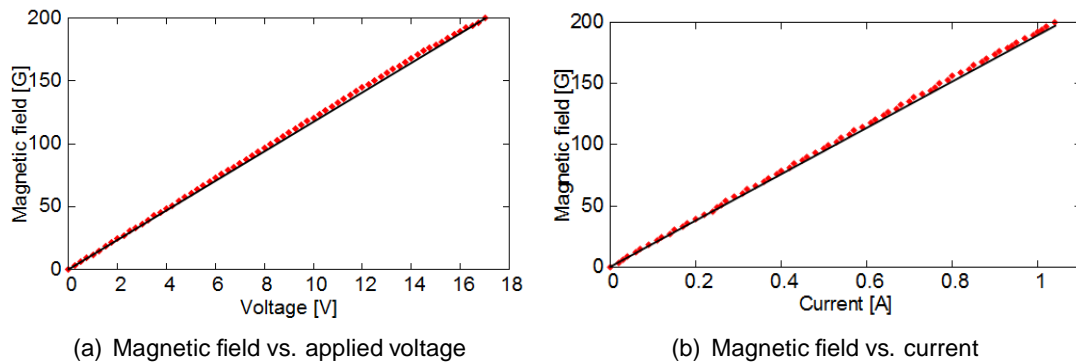


Figure 4.8: Comparison between theoretical (solid line) and measured (diamonds) DC magnetic field for the coil #1. The theoretical curve is computed from (D.10).

With regard to alternating current, the magnetic field produced by a solenoid is constantly changing in phase with the applied current. As a first approximation we can write,

$$B = \frac{\mu_0 N}{L} I_0 \cos(\omega t) \quad (4.3)$$

The solenoid can be considered a series RL circuit the behaviour of which is reviewed in the last section of the Appendix D. Figure 4.9 shows the magnetic field produced by the solenoid as a function of the frequency and different input voltage amplitudes. Note that the measured magnetic field is shown as a peak value for a given frequency, as provided by the magnetometer.

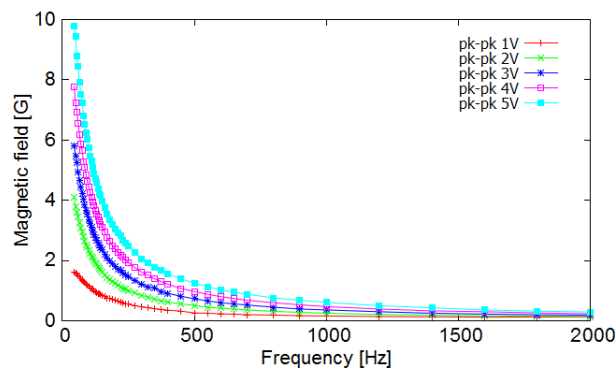


Figure 4.9: AC magnetic field as a function of the frequency for different amplitudes.

4.1.4. Magnetometer

A magnetometer supplied by *AlphaLab Inc.* was used to measure the magnetic flux density inside the solenoid during the experiments. In particular, the available magnetometer was the model High Stability DC Magnetometer, which is capable of measuring both DC and AC

magnetic fields in 1-axis, from 0.01 up to 199.99 G with 0.01 G resolution, while indicating the field polarity. The frequency range for AC magnetic field measurements is 45 Hz to 2000 Hz. Accuracy is $\pm 2\%$ of the reading for DC and $\pm 3\%$ for AC.

The probe's sensor is located in the air gap within the solenoid below the sample bracket and oriented such that it measures the magnetic field component along a direction parallel to the crack (i.e., parallel to the revolution axes of the solenoid and the symmetry axis of the sample, the z axis). The reader can refer to Appendix E for further details on the magnetometer operation and sensor orientation, as provided in the magnetometer datasheet. Besides, even though the calibration is certified by the manufacturer for a period comprising the completion of the author's master thesis, a sensor with a well-known response at low-field range was used to discard measurement anomalies. The results and relevant comments in this regard are also shown in the previously mentioned appendix.

4.2. DC experiment set-up

The DC magnetic field z -axis component is to be measured by a Hall sensor mounted transversely below the centre of the sample (Fig. 4.10) in each of the following DC experimental conditions:

Case DC.1: Sample placed on the support with no ferrofluid in the crack and no electric current being supplied to the coil.

Case DC.2: Sample placed on the support with no ferrofluid in the crack, while DC power is being supplied to the coil.

Case DC.3: Sample placed on the support with a certain amount of ferrofluid in the crack, while DC power is being supplied to the coil (the ferrofluid is thus being magnetized).

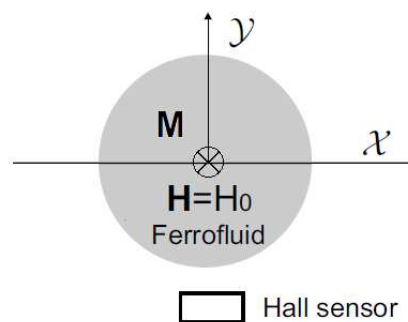


Figure 4.10: MEDD DC experimental set-up: Hall sensor position with respect to the ferrofluid. M is the ferrofluid magnetization within the crack (modelled as a cylinder) and H is the applied magnetic field along the solenoid revolution axis.

Table 4.3 summarizes the above mentioned conditions.

Table 4.3: Summary of experimental conditions in DC tests.

Case	Sample on support	Ferrofluid in crack	DC power supplied to coil
DC.1	YES	NO	NO
DC.2	YES	NO	YES
DC.3	YES	YES	YES

Once the DC experimental set is ready, the test procedure consists of the following steps:

1. Set the magnetometer to measure DC magnetic fields.
2. Place the sample on the support and set the magnetic field reading to zero by applying the appropriate offset in the magnetometer (case DC.1). Leave the bracket oriented in this direction for the remaining steps.
3. Switch on the power source to supply DC power to the coil at the selected voltage. Record the magnetic field reading in the magnetometer (case DC.2). Switch off the power source.
4. Remove the test-piece and apply the ferrofluid homogeneously in the crack with the precision pipette. Relocate the test-piece on the sample support.
5. Switch on the power source to supply DC power to the coil at the selected voltage. Record the magnetic field reading in the magnetometer (case DC.3).

The process from step 3 to 5 can be repeated as many times as desired using different values of DC voltage, i.e., different values of magnetic field generated by the coil.

4.3. AC experiment set-up

With regard to alternating current, again the z -axis component of the magnetic field is to be measured by a Hall sensor (Fig. 4.11), although a slight variation of the previous section's procedure is presented. Only two conditions are necessary in this case, since no offset is required for the magnetometer switched into AC position. They are the following:

Case AC.1: Sample placed on the support with no ferrofluid in the crack, while AC power is being supplied to the coil.

Case AC.2: Sample placed on the support with a certain amount of ferrofluid in the crack, while AC power is being supplied to the coil (the ferrofluid is thus being magnetized).

Table 4.4 summarizes these conditions.

Table 4.4: Summary of experimental conditions in AC tests.

Case	Sample on support	Ferrofluid in crack	AC power supplied to coil
AC.1	YES	NO	YES
AC.2	YES	YES	YES

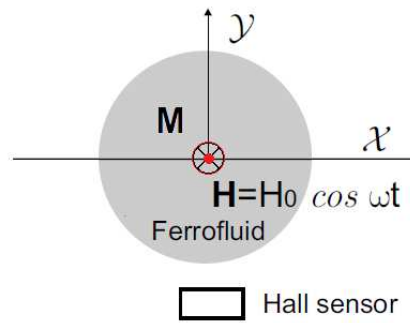


Figure 4.11: MEDD AC experimental set-up: Hall sensor position with respect to the ferrofluid. M is the ferrofluid magnetization within the crack (modelled as a cylinder) and H is the applied alternating magnetic field, which in this case oscillates along the solenoid revolution axis.

Once the AC experimental set is ready, the test procedure consists of the following steps:

1. Set the magnetometer to measure AC magnetic fields.
2. Place the sample on the support. Leave the bracket oriented in this direction for the remaining steps.
3. Switch on the power source to supply AC power to the coil at the selected amplitude and frequency (case AC.1). Record the magnetic field phase reading, with respect to the input voltage phase, in the oscilloscope. Set both oscilloscope x -counters at a fixed reference point of the magnetic field's sinusoidal signal, e.g., a point at which crosses the x -axis.
4. Remove the test-piece and apply the ferrofluid homogeneously in the crack with the precision pipette.
5. Relocate the test-piece on the sample support. Record the new magnetic field phase reading with respect to that of the input voltage. Adjust one of the counters to the new reference point of the magnetic field signal shown in the oscilloscope (case AC.2) and record the relative difference in phase with respect to the previous case (case AC.1).

The process from step 3 to 5 can be repeated as many times as desired using different values of frequency and/or input voltage amplitude, i.e., different values of magnetic field generated by the coil.

CHAPTER 5. RESULTS AND DISCUSSION

5.1. DC magnetization

In this section, a theoretical development is presented to calculate analytically the magnetic field due to presence of ferrofluid in the crack under a DC magnetic field. Results are presented for the ferrofluid the characteristics of which are detailed in Section 4.1.1. The following hypotheses are assumed:

1. The AA 2024-T3 of the test specimen is a diamagnetic material.
2. The magnetic fluid is monodisperse, i.e., the magnetic particles are all identical in composition, properties, dimensions and shape (assumed to be spherical).
3. The ferrofluid is assumed to be a dilute colloidal suspension (i.e., the magnetic particles occupy less than 10% of the total volume of the magnetic fluid).
4. Each magnetic particle is a single magnetic domain (i.e., it is an entity with a single magnetic moment), and thus behaves as a single magnetic dipole. Besides, the particles are non-interacting.
5. The magnetic moments of a certain percentage of the particles in the crack are aligned with the longitudinal axis of the crack when subjected to an applied magnetic field.
6. The magnetization is homogeneous within the ferrofluid.
7. There is no other source of magnetic noise than the Earth, and the average modulus of the Earth's magnetic field is 0.5 G (0.05 mT). For simplicity, by applying appropriate offset, it is assumed that it has no component along the longitudinal axis of the crack.

Hypothesis 1 was confirmed by measurements under DC.2 test condition, which proved that the sample does not modify the background magnetic field. With regard to the hypothesis 2, the magnetic particles of magnetic fluids are commonly spherical [36]. Hypotheses 3, 4 and 5 may be used to compute the volume saturation magnetization M_{sat} of the ferrofluid. In this case, though, it is provided by the manufacturer (Table 4.1). Hypothesis 4 is very convenient and coherent with the values of particle diameters and critical diameters for the studied ferrofluid. In particular, for magnetic fluids with particle diameters ranging from 5 to 15 nm, each particle typically consists of a single magnetic domain [36]. Hypothesis 5 is coherent with the concept of magnetization of ferrofluids introduced in Section 3.2. Hypothesis 6 will be discussed in the following lines. Finally, hypothesis 7 is acceptable because the background magnetic field in the direction of the crack's longitudinal axis can be set to null by applying the appropriate offset.

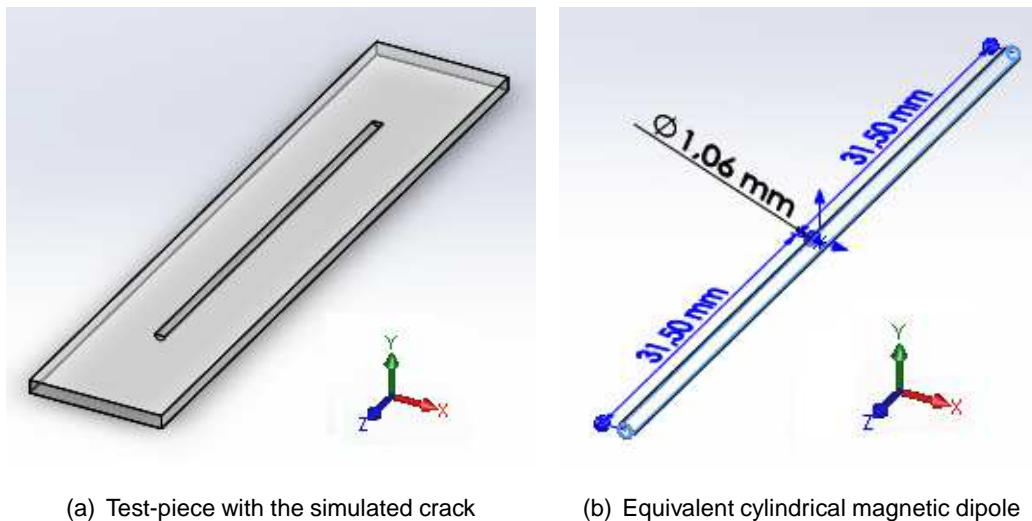
From the basis of hypotheses 2 to 6, assuming the magnetization to be homogeneous within the ferrofluid, the magnetic fluid inside the crack is modelled as a single cylindrical

magnetic dipole with selected dimensions for it to have an equivalent volume to that of the ferrofluid deposited inside the crack: 0.53 mm radius r and 31.5 mm semi-length a . The mass of ferrofluid accumulated into this model is around 80 mg. Table 5.1 summarizes this data and that of the simulated crack.

Table 5.1: Geometric characteristics of the simulated crack and equivalent magnetic dipole. The simulated crack is a half cylinder, whereas the magnetic dipole is a cylinder with equivalent volume.

Simulated crack		
Characteristic	Symbol	Value
Semi-length	a_{crack}	31.5 mm
Radius	r_{crack}	0.75 mm
Volume	V_{crack}	$5.56 \cdot 10^{-8} \text{ m}^3$
Equivalent magnetic dipole		
Characteristic	Symbol	Value
Semi-length	a_{dipole}	31.5 mm
Radius	r_{dipole}	0.53 mm
Volume	V_{dipole}	$5.56 \cdot 10^{-8} \text{ m}^3$

Figures 5.1(a) and 5.1(b), respectively, show the crack simulated on the test object and the sketch of the equivalent dipole model representing the ferrofluid inside the crack, together with the reference system used in this research. The origin of the reference system is the centre of the dipole. The z -axis is coincident with the revolution axis of the dipole, parallel to the longitudinal axis of the sample and the revolution axes of the solenoid. The x -axis is perpendicular to the z -axis and parallel to the specimen surface. The y -axis is perpendicular to the x and z -axes, pointing upwards of the specimen surface.



(a) Test-piece with the simulated crack

(b) Equivalent cylindrical magnetic dipole

Figure 5.1: Models of the test-piece and equivalent cylindrical magnetic dipole. The origin of the reference system is the centre of the dipole

This equivalent magnetic dipole has an associated magnetic field resulting from the integration of the magnetic fields produced by each of the aligned dipole moments corresponding to the magnetized particles within the crack. The density of this induced magnetic dipole moment is expressed by the magnetization of the ferrofluid, which in turn describes

the way the material changes the magnetic field (Fig. 5.2) and can be used to calculate the forces that result from those interactions.

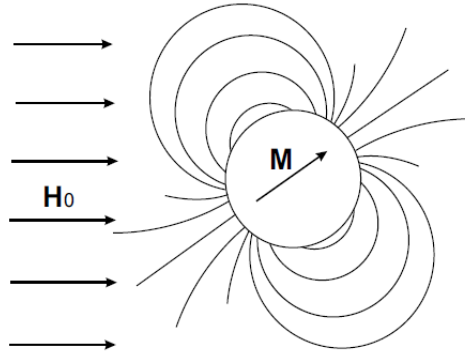


Figure 5.2: Magnetization of a magnetic dipole as a result of an external magnetic field.

The purpose of the custom-made solenoid is to apply an external magnetic field H_{out} in the air gap in which the sample with the crack is placed to force spin alignment. Figure 5.3 shows the cylinder magnetic dipole equivalent to the ferrofluid under this condition. It is then necessary to obtain the field produced by the ferrofluid by relating it to the applied field.

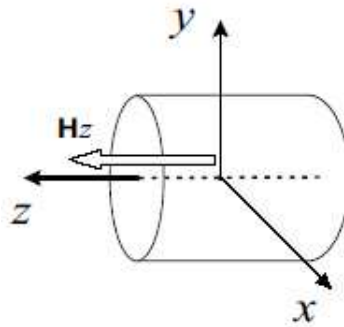


Figure 5.3: Ferrofluid cylinder in a magnetic field.

Any system possessing a net magnetic dipole moment m will produce a dipolar magnetic field in the surrounding space. This magnetic field can be calculated with the magnetostatic Maxwell equations

$$\vec{B}(\vec{r}) = \vec{B}_I(\vec{r}) + \vec{B}_{II}(\vec{r}) = \mu_0 \vec{M}(\vec{r}) - \mu_0 \nabla \phi^*(\vec{r}) \quad (5.1)$$

$$\nabla \cdot \vec{B}(\vec{r}) = 0 \quad (5.2)$$

$$\nabla \times \vec{H}(\vec{r}) = 0 \quad (5.3)$$

where \vec{B} is the magnetic flux density vector, \vec{r} is the position vector, μ_0 is the free space permeability constant, \vec{M} is the material magnetization, ϕ^* is the scalar potential (a function of \vec{r}), and \vec{H} is the magnetic field vector.

Inside the equivalent magnetic dipole, the first term on the right hand side (r.h.s.) of (5.1) depends on the magnetization of the ferrofluid. However, the region of interest is that outside the dipole. Far from any source of magnetic noise, this term corresponds to the Earth's magnetic field, with an average modulus of 0.5 G (0.05 mT). Nevertheless, as mentioned at the beginning of this section, this term is assumed to have null component in the z -axis. From now on, the second term on the r.h.s. of (5.1) will be referred to as the magnetic field associated to the presence of magnetic fluid in the crack. This term can be calculated with the following expression [54]

$$\vec{B}_{II}(\vec{r}) = -\mu_0 \nabla \phi^*(\vec{r}) = -\mu_0 \nabla \frac{1}{4\pi} \int_{\Omega} \vec{M}(\vec{r}') \frac{\vec{r} - \vec{r}'}{|\vec{r} - \vec{r}'|^3} dV' \quad (5.4)$$

where \vec{r}' is the position vector of a differential magnetic dipole. For a cylindrical dipole, and considering the reference system shown in Figure 5.1(b), (5.4) becomes

$$\begin{aligned} \vec{B}_{II}(\vec{r}) = & -\frac{1}{4\pi} \mu_0 M \pi R^2 \left[\left(\frac{x}{(x^2 + y^2 + (z+a)^2)^{3/2}} - \frac{x}{(x^2 + y^2 + (z-a)^2)^{3/2}} \right) \hat{i} \right. \\ & + \left(\frac{y}{(x^2 + y^2 + (z+a)^2)^{3/2}} - \frac{y}{(x^2 + y^2 + (z-a)^2)^{3/2}} \right) \hat{j} \\ & \left. + \left(\frac{z+a}{(x^2 + y^2 + (z+a)^2)^{3/2}} - \frac{z-a}{(x^2 + y^2 + (z-a)^2)^{3/2}} \right) \hat{k} \right] \quad (5.5) \end{aligned}$$

where a is the semi-length of the crack. From (5.5), the magnetic field due to the magnetic fluid was computed in the plane perpendicular to the crack/dipole axis: the xy -plane at the crack centre, i.e., the plane $z = 0$. The magnetic field created by the dipole in the xy -plane has only component along the z -axis, thus the magnetic field modulus is equal to the magnitude of the magnetic field z component

$$\vec{B}_{II}(\vec{r}) \Big|_{z=0} = B_z \hat{k} = -\frac{1}{4\pi} \mu_0 M \pi R^2 \left[\frac{2a}{(a^2 + x^2 + y^2)^{3/2}} \right] \hat{k} \quad (5.6)$$

Before proceeding with the calculation of the magnetic field produced by the ferrofluid, it is necessary to compute its magnetization M due to its exposure to a certain magnetic field on the basis of the theory presented in Section 3.4.3. The Langevin parameter is given by (3.34)

$$\alpha = \frac{m \mu_0 H}{k_B T}$$

with μ_0 and k_B constant values, the temperature T set at 20°C (293.15 K) and the magnetic moment m of the particle given by the ferrofluid properties, the only parameter that varies is the applied magnetic field H .

Computing now the non-dimensional magnetization with (3.33) for several values of the Langevin parameter (i.e., several applied magnetic fields), the curves in Figures 5.4(a)

and 5.4(b) result, respectively, for the whole range of applied magnetic fields up to ferrofluid saturation and those achievable with the available instrumentation. From Figure 5.4 it can be noted that the equilibrium magnetization of the magnetic fluid increases linearly with the strength of the applied field, for relatively small field magnitudes.

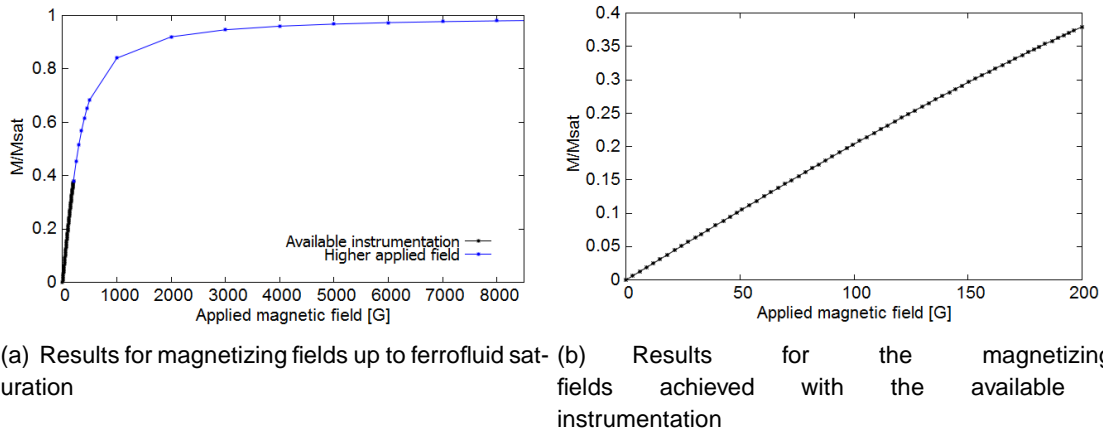


Figure 5.4: Non-dimensional magnetization as a function of the applied magnetic field. Solutions are for the following input data: $m = 2.53 \cdot 10^{-19} \text{ A} \cdot \text{m}^2$, $T = 293.15 \text{ K}$.

Multiplying by the ferrofluid saturation magnetization as provided by the manufacturer, the above shown curves can be expressed dimensionally (Figures 5.5(a) and 5.5(b)).

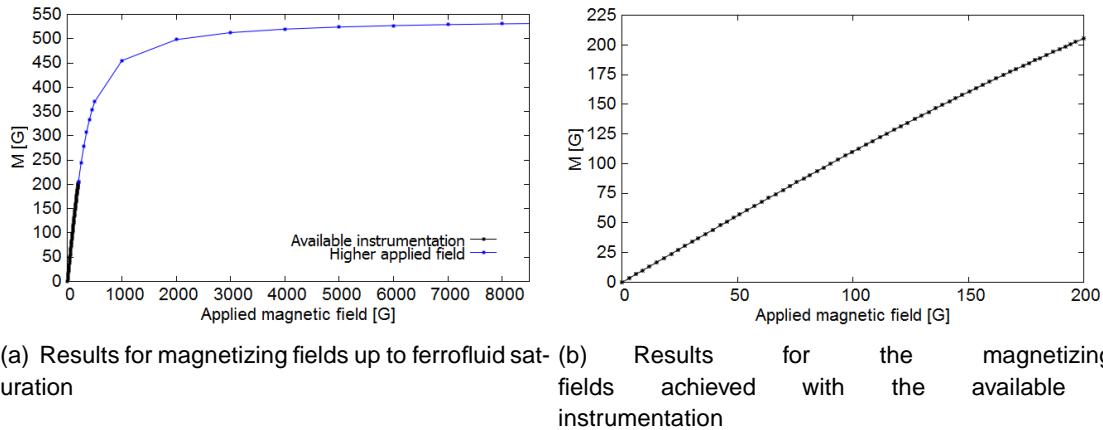


Figure 5.5: Dimensional magnetization as a function of the applied magnetic field. Solutions are for the following input data: $m = 2.53 \cdot 10^{-19} \text{ A} \cdot \text{m}^2$, $T = 293.15 \text{ K}$, $M_{sat} = 531 \text{ G}$.

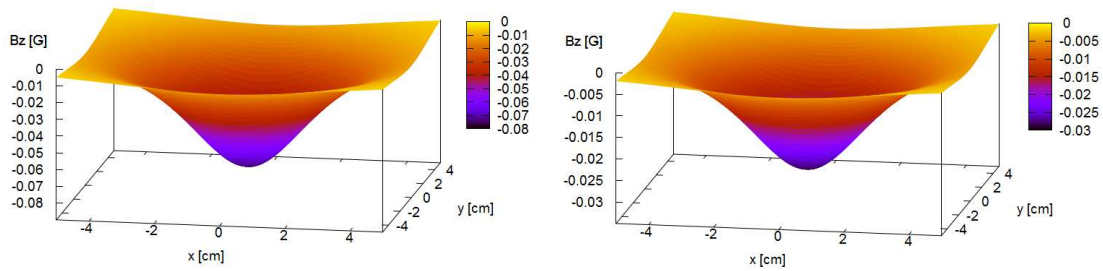
The values of the maximum magnetization obtained with the available instrumentation and the ferrofluid saturation magnetization that would be obtained by applying a higher external field are shown in Table 5.2 below.

Table 5.2: Ferrofluid magnetization.

Case	Symbol	Value
Max. magnetization	$0.38M_{sat}$	205 G
Saturation magnetization	M_{sat}	531 G

Introducing these magnetization values into (5.6) and solving for $z = 0$ (i.e., at the centre of the equivalent magnetic dipole), the theoretical magnetic field that the ferrofluid would

produce in the surrounding space is obtained. For a dipole with the selected dimensions, Figures 5.6(a) and 5.6(b) show the 3D plots corresponding to the magnetic field described by (5.6) for both cases.



(a) Results for magnetizing fields up to ferrofluid saturation

(b) Results for the magnetizing fields achieved with the available instrumentation

Figure 5.6: 3D plot of the magnetic field variation in the surrounding space of the magnetic dipole.

Note in Figures 5.6(a) and 5.6(b) that the magnetic field induced in the xy plane when the ferrofluid within the crack is magnetized is negative. The reason for this is that the magnetic moments of the magnetic particles align with the z -axis (i.e., with the lines of the applied magnetic field along the crack/dipole longitudinal axis), such that the magnetic field is reinforced inside the dipole. In this configuration, the lines of the magnetic field of the ferrofluid exit the dipole through its tip in the region of positive z (north pole) and enter the dipole through its tip in the region of negative z (south pole), closing the loop. This is the reason why the z component of the induced magnetic field of the ferrofluid is negative outside the dipole in the xy plane

The maximum variation of the magnetic field introduced by the dipole is at the origin of the reference system, i.e., at the centre of the dipole. The Hall sensor, though, is slightly displaced vertically (a few millimeters below the test-piece) and thus the expected value is lower than the former on the order of mG. Figures 5.7(a) and 5.7(b) show the expected variation in the sensed magnetic field for the analytical and experimental results as a function of the distance to the crack axis and Table 5.3 summarizes these values. The sensor resolution is actually 0.01 G, meaning that this variation should not be significant from an experimental point of view.

Table 5.3: Maximum field variation at both the dipole's centre and the sensor position.

At the dipole's centre		
Case	Symbol	Value
Max. magnetization	$\Delta B_{z,max_1}$	-0.029 G
Saturation magnetization	$\Delta B_{z,sat_1}$	-0.075 G
At the sensor position		
Case	Symbol	Value
Max. magnetization	$\Delta B_{z,max_2}$	-0.028 G
Saturation magnetization	$\Delta B_{z,sat_2}$	-0.073 G

In light of these results, theory states that a certain variation in the magnetic field in the vicinity of the crack should be detectable with the available means. A series of experimental

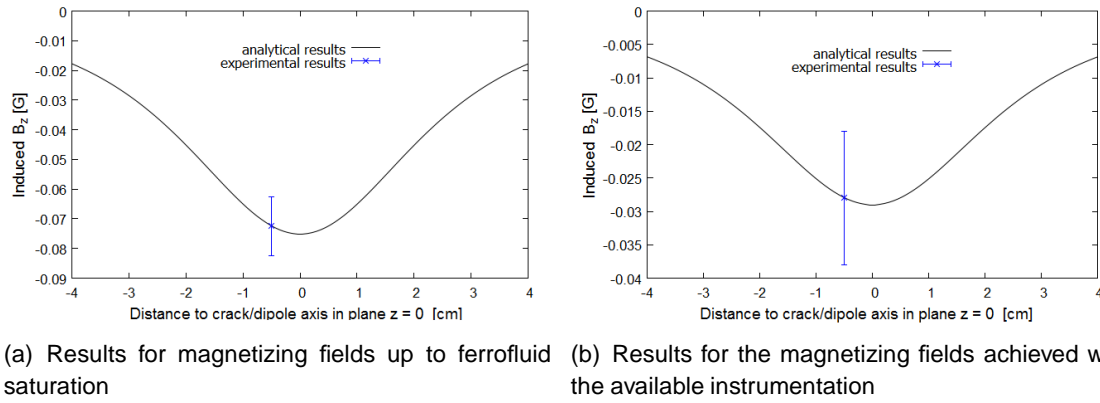


Figure 5.7: Magnetic field variation as a function of the distance to the crack. The expected experimental result is shown at the sensor position, $r = -5$ mm.

tests were performed by the author with the instrumentation presented in Chapter 4 in order to compare the latter to the theoretical ones. In particular, this process was performed with DC voltages ranging from 1 to 17 V in steps of 1 V until reaching the magnetometer saturation at nearly 200 G, point at which the maximum variation should be introduced by the ferrofluid accumulated in the crack. Contrary to what expected, a certain oscillation in the magnetometer reading during the tests, probably due to Brownian motion of the particles within the ferrofluid and possible imperfections of the experimental set (e.g., non-perfect alignment of the test-piece with the revolution axis of the solenoid or incorrect sensor positioning with respect to the former), did not allow acquiring a definitive value of the measured magnetic field and thus no comparison with the theoretical results can be provided. It is worth noting, though, that discrepancies between the analytical and experimental results may be, aside from the limitations of the experimental set, due to overly optimistic assumptions with regard to the ferrofluid characteristics. For instance, the fact that no saturation is reached within the ferrofluid implies that the thermal effects may play an important role in the physical process.

Remarkable is the fact that very weak field variations are to be detected in the frame of relatively high applied magnetic fields. This entails that a greater sensitivity and resolution than that offered by the magnetometer available during the realization of this thesis might be needed to reliably detect the variations in magnitude of the magnetic field. By increasing the magnetometer range to values close to the necessary for reaching the ferrofluid saturation magnetization, the chances of detecting the perturbation would increase considerably. In this sense, probably more sophisticated, expensive equipment able to simultaneously generate a magnetic field strong enough to magnetize the ferrofluid and to measure the variations in magnetic field would be necessary.

5.2. AC magnetization

This section is focused on the dynamic magnetization of the ferrofluid within the crack. The same hypotheses assumed in the previous section apply for this case, plus a further assumption regarding the particle relaxation time. For simplicity, the Brownian relaxation

time is considered to dominate the physical process of relaxation.

The idea arose as an alternative to the method based on the DC magnetization. At very low frequencies, the phenomenon is most similar to that of DC. In this case, the magnetization of the ferrofluid within the crack follows the $M(H)$ curve given by the Langevin function (3.33). As long as the AC field is small, the induced AC moment is given by (3.36) which can be equivalently written in dimensional form as follows

$$M_{AC} = \frac{dM}{dH} H_{AC} \sin(\Omega t) \quad (5.7)$$

where H_{AC} is the amplitude of the driving magnetic field, Ω is the driving frequency and $\chi = dM/dH$ is the magnetic susceptibility introduced in Section 3.2.. From (5.7) appears that this phenomenon is very sensitive to small changes in the magnetization $M(H)$ and not to its absolute value, making small magnetic shifts detectable even when the absolute moment is large [55].

At higher frequencies than those considered above, the AC magnetization of the ferrofluid within the crack does not follow along the DC magnetization curve due to dynamic effects but may lag behind the drive field. As previously stated in (3.10), AC magnetic susceptibility is a complex quantity with magnitude χ and a certain phase shift φ relative to the drive signal which can be written as follows

$$\chi = \sqrt{\chi'^2 + \chi''^2} \quad (5.8)$$

$$\varphi = \arctan\left(\frac{\chi''}{\chi'}\right) \quad (5.9)$$

where χ' is the slope of the $M(H)$ curve discussed above in the limit of low frequency in conditions similar to DC, given by (3.9), and χ'' indicates dissipative processes in the ferrofluid due to relaxation mechanisms.

The characteristic time of the system is given by the Brownian relaxation time, defined by (3.26)

$$\tau_B = \frac{3V\eta}{k_B T}$$

The system's relaxation time determines the maximum frequency at which the particles within the ferrofluid may relax when subjected to an external oscillating magnetic field

$$\Omega_{max} = \frac{1}{\tau_B} \quad (5.10)$$

The initial susceptibility can be computed from (3.11)

$$\chi_0 = \frac{M_{sat}\mu_0 m}{3k_B T}$$

The results of these parameters for the studied ferrofluid are listed in Table 5.4, whereas Figure 5.8 shows both the real and imaginary components of the complex susceptibility as a function of the drive signal's frequency (i.e., the magnetic field frequency).

Table 5.4: Parameters for the calculation of the AC magnetic susceptibility.

Quantity	Symbol	Value
Characteristic time	τ_B	$1.009 \cdot 10^{-5}$ s
Maximum frequency	Ω_{max}	99100 Hz
Initial susceptibility	χ_0	1.13

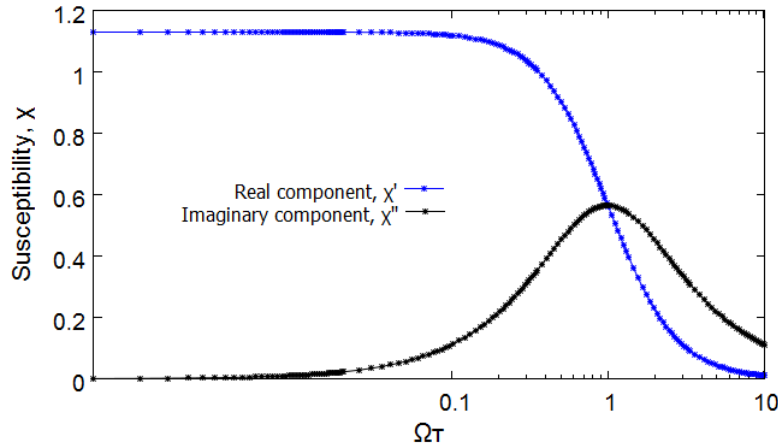


Figure 5.8: Real and imaginary components of the complex susceptibility for the studied ferrofluid as a function of the drive signal's frequency. The system's characteristic time τ is $1.009 \cdot 10^{-5}$ s, the initial susceptibility χ_0 is 1.13 and the temperature T is 293.15 K. Note that the x -axis is presented in logarithmic scale.

The frequency Ω_{max} is that at which there is a peak of the imaginary component of the susceptibility shown in Figure 5.8. That is the maximum frequency that the applied magnetic field might adopt while allowing the particles within the ferrofluid for complete relaxation. Beyond that frequency, the particle magnetic moments would not be able to follow the applied magnetic field and would start a sort of precession motion. This effect randomizes the particles orientation within the ferrofluid in what is known as demagnetization of the ferrofluid.

Equation (5.9) allows computing the phase lag that the magnetic field induced by the ferrofluid in the crack may have with respect to the reference applied field as a function of the applied frequency. The solution is shown in Figure 5.9(a) for frequencies ranging from 0 to Ω_{max} . The frequency range of the magnetometer used in this research, though, is limited from 45 to 2000 Hz. Figure 5.9(b) shows in detail the theoretical phase shift that would be obtained within that range.

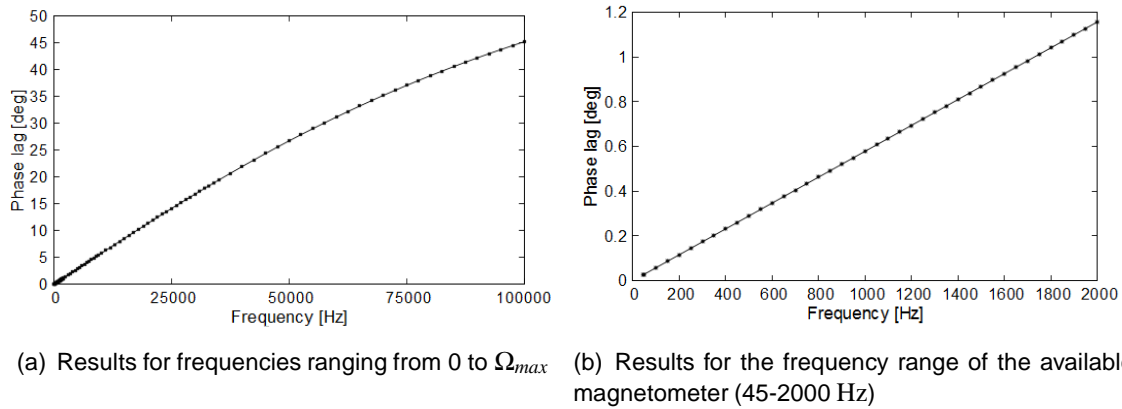


Figure 5.9: Phase lag induced due to the presence of ferrofluid.

The expected value at the maximum detectable frequency (2 kHz) is about 1 degree, a rather small value for its detection with the available instrumentation. The phase lag between the drive signal and the one induced by the ferrofluid is independent of the volume of ferrofluid accumulated in the surface crack. However, the magnitude of the signal detected with the available magnetometer does depend on the amount of ferrofluid deposited in the flaw. Besides, when the ferrofluid is inserted into the crack, the noise in the magnetic field signal acquired by the Hall sensor and transferred to the oscilloscope makes it difficult to detect the small difference in the signal's phase by means of the counters on the oscilloscope (i.e., no precise adjustment of the counters is possible with the acquired signal). Fig. 5.10 shows how the signal should shift and cross the x -axis at a different time after the deposition of ferrofluid into the crack. Counter X2 would then be moved to the point at which the new signal due to the presence of ferrofluid crosses the x -axis, and that would allow measuring the difference with respect to the reference point set by counter X1.

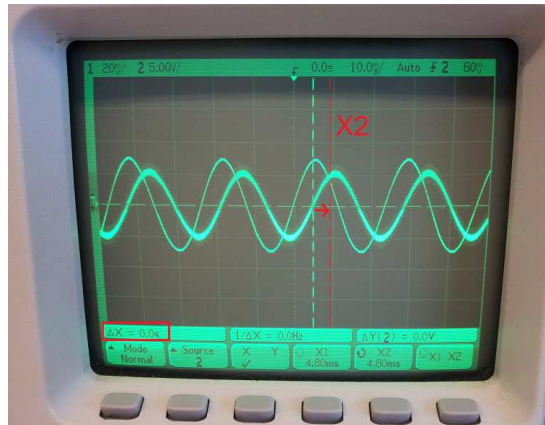


Figure 5.10: Proposed method for measuring the phase lag induced due to the presence of ferrofluid inside the defect.

In contrast, at frequencies near to that of the system Ω_{max} , the phase lag between the magnetic field induced by the ferrofluid and that of the applied magnetic field reaches a value of about 45 degrees and it should indeed be detectable with the proposed method if the frequencies close to Ω_{max} were within the magnetometer range. An appropriate, more sophisticated and probably more expensive data acquisition equipment would certainly enable detection of this shift in the phase of the signal.

CHAPTER 6. CONCLUSIONS

This chapter presents, in Section 6.1., the conclusions drawn with regard to the main objectives after all the performed tasks and experiments. After that, Section 6.2. presents the next steps to be done if this work is to be continued and a list of future research ideas.

6.1. Achieved objectives

In this thesis, an innovative NDT technique concept for the detection of surface cracks in non-ferromagnetic materials has been studied both theoretically and experimentally. The technique is based on the local magnetic field variation due to the deposition of a ferrofluid consisting of magnetic nanoparticles in the test-piece surface.

The final objective of the conducted study was to assess the feasibility of the proposed concept. For this purpose, a theoretical study has been carried out regarding DC and AC magnetization of the ferrofluid, which shows that a magnetic field variation due to the presence of ferrofluid in the crack may be detectable by appropriate means under certain conditions. When the technique was conceived, the first intention was to test if the proposed NDT concept would allow detection of surface cracks with the fail-safe and damage tolerance reference crack dimensions or even smaller, given that one of the most important target applications of this innovative technique would be aircraft skin panel inspection. A preliminary series of analytical results, though, showed that the magnetic field induced by the ferrofluid was rather weak for the signal to be detected with the available means for these target crack dimensions. Notwithstanding this fact, the research had still great scientific interest and a crack of larger dimensions was used in this study to compare the theoretical results to the experimental ones obtained with the available instrumentation. The experimental results suggest that the available instrumentation may not be appropriate to reproduce the optimal conditions for the signal to be detected both accurately and precisely enough to confirm the theoretical results. Results show, for the DC version of the proposed technique, that a variation of the order of centi Gauss (cG) may be detected in the vicinity of the crack in which the ferrofluid is deposited.

Concerning the version of the concept based on AC magnetization of the ferrofluid, it was proposed as an alternative to the DC version mentioned above and consisted in exploiting the magnetic field phase shift that the ferrofluid within the cracks may produce with respect to the drive signal (i.e, that of the applied magnetic field). In this case the theoretical results showed that the necessary range of frequencies to achieve the optimal detection conditions was far from the capabilities of the available instrumentation. Nevertheless, as stated by the theoretical results, a variation in phase of up to 45 degrees between the magnetic field induced by the ferrofluid deposited in the crack and the drive magnetic signal would exist at frequencies close to the system's characteristic frequency. In this sense, an instrumentation set with appropriate characteristics of frequency range and sensitivity should indeed be able to detect the expected variation in the magnetic field signal phase.

In short, promising theoretical results state that crack detection would be feasible with this method provided that a more sensitive sensor and/or another ferrofluid with magnetic particles featuring much more intense saturation magnetization are used.

6.2. Future Work

Thanks to the first theoretical study done over the proposed technique concept and provided the results of this work are satisfactory, the ultimate objective of the research would be to develop the proposed technique, striving to meet the accuracy, reliability and safety requirements of NDT applications in the aerospace and air transport industries (e.g., aircraft skin panel inspection), while trying also to reduce the inspection costs, compared to the most common NDT methods used at present day. Commercial availability is an important consideration when reviewing potential NDT techniques, since there are a large number of methods which could in principle detect the relatively large defect sizes necessary to find, but the engineering effort and expense to convert them from laboratory systems into robust, reliable field units is considerable.

This first approach put some light over some issues to upgrade. This way, some variations to the proposed method may prove promising. A proposed solution that may be interesting would be to base the detection of defects in signal processing. To achieve this, a deeper and detailed study of the signals produced by the accumulation of ferrofluid in different types of surface discontinuities is imperative. After appropriate data acquisition and filtering, the goal would be to try to identify patterns in the magnetic field signals and correlate them with the dimensions and morphology of the defect. Ideally, the existence of these patterns, after the appropriate detection and signal processing, would not only identify the presence of cracks but also their size and shape in a way similar to that performed by algorithms in already existing techniques such as Process Compensated Resonance Testing, briefly introduced in Section 2.2.

Another solution would be to implement the already existing *Vibrating Sample Magnetometer* (VSM), a device the operation of which is extensively documented in references [42] and [27]. This method, however, may entail certain limitations as for the development of an NDT technique for out-of-the-lab applications since vibration of the sample is required to enable the detection of the signals due to ferrofluid accumulation.

On the contrary, AC magnetometry introduced in reference [55] does not require the vibration of the test-piece and appears to be appropriate to measure very slight variations of magnetic signals due to the presence of a ferrofluid, so its application should certainly be considered if the work presented in this thesis is to be continued.

BIBLIOGRAPHY

- [1] W. D. Callister and D. G. Rethwisch. *Materials science and engineering: an introduction*. 2007.
- [2] S. Gosselin. *Aircraft design to operational cost*. Technical report, DTIC Document, 2000.
- [3] J. T. Schmidt, K. Skeie, and P. McIntire. *Magnetic particle testing*. American Society for Nondestructive Testing, 1989.
- [4] Zuuk Inspection. *History of Non-Destructive Testing*, 2011.
- [5] P. Cawley. Non-destructive testing-current capabilities and future directions. *Proceedings of the Institution of Mechanical Engineers, Part L: Journal of Materials Design and Applications*, 215(4):213–223, 2001.
- [6] R. C. McMaster and S. A. Wenk. A basic guide for management's choice of non-destructive tests. *Special Technical Publication*, (112):3–80, 1951.
- [7] S. A. Wenk, R. C. McMaster, and P. McIntire. *Choosing NDT: Applications, costs, and benefits of nondestructive testing in your quality assurance program*. American Society for Nondestructive Testing (Columbus, OH), 1987.
- [8] S. Ness, C. N. Sherlock, P. O. Moore, and P. McIntire. *Nondestructive testing overview*. American Society for Nondestructive Testing, 1996.
- [9] The engineer. *Non-destructive testing in the aerospace industry*, 2011.
- [10] M. W. Allgaier, S. Ness, P. McIntire, and P. O. Moore. *Visual and optical testing*. American Society for Nondestructive Testing, 1993.
- [11] R. C. McMaster. *Liquid penetrant tests*. American Society for Nondestructive Testing. American Society for Metals, 1982.
- [12] J. Blitz. *Electrical and magnetic methods of non-destructive testing*, volume 3. Springer, 1997.
- [13] L. E. Bryant. *Nondestructive testing handbook*. volume 3: Radiography and radiation testing. 1985.
- [14] Acoustic impedance. Wikipedia.
- [15] D. E. Bray, A. S. Birks, and R. E. Green Jr. *Ultrasonic testing applications in the transportation industries-part 1*, 1991.
- [16] R. K. Stanley, P. O. Moore, and P. McIntire. Special nondestructive testing methods, vol. 9 of. *Nondestructive Testing Handbook*, 1995.
- [17] C. Hobbs and A. Temple. The inspection of aerospace structures using transient thermography. *British Journal of Non-Destructive Testing*, 35(4):183–189, 1993.

- [18] A. Migliori and J. L. Sarrao. *Resonant ultrasound spectroscopy*. Wiley New York, 1997.
- [19] L. Hunter and R. Nath. Process compensated resonant testing: Lessons learned about a new, but maturing ndt method that detects structural degradation of parts, 2008.
- [20] J. Schwarz, J. Saxton, and L. Jauriqui. Process compensated resonant testing in manufacturing process control. *Materials evaluation*, 63(7):736–739, 2005.
- [21] C. D. Wells. The commercial role of ndt in the context of a changing world. *Insight*, 36(5):334–341, 1994.
- [22] Inc. Global Industry Analysts. Nondestructive test equipment: A global strategic business report, 2011.
- [23] Frost and Sullivan. World ndt inspection services market - an indestructible future, 2011.
- [24] A. Khalid. Review of the ndt market and performance of ndt companies operating in the uk. *Insight*, 41(4):232–43, 1999.
- [25] C. Scherer and A. M. Figueiredo Neto. Ferrofluids: properties and applications. *Brazilian Journal of Physics*, 35(3A):718–727, 2005.
- [26] R. E. Rosensweig. Ferrofluids introduction. *Encyclopedia of Materials: Science and Technology*, 2001.
- [27] S. May. Rotational relaxation dynamics of ferrofluid systems. Technical report, The University of Hull.
- [28] R. E. Rosensweig. *Ferrohydrodynamics*, 1985.
- [29] F. Weinhold. Chemistry: A new twist on molecular shape. *Nature*, 411(6837):539–541, 2001.
- [30] S. W. Charles, J. Popplewell, and E. P. Wohlfarth. *Ferromagnetic materials*, vol. 2north-holland, 1980.
- [31] J. Depeyrot, G. J. da Silva, C. R. Alves, E. C. Sousa, M. Magalhães, A. M. Figueiredo Neto, M. H. Sousa, and F. A. Tourinho. Static magneto optical birefringence of new electric double layered magnetic fluids. *Brazilian journal of physics*, 31(3):390–397, 2001.
- [32] R. Massart, E. Dubois, V. Cabuil, and E. Hasmonay. Preparation and properties of monodisperse magnetic fluids. *Journal of Magnetism and Magnetic Materials*, 149(1):1–5, 1995.
- [33] Specific gravity. Wikipedia.
- [34] H. W. Müller and A. Engel. Dissipation in ferrofluids: Mesoscopic versus hydrodynamic theory. *Physical Review E*, 60(6):7001, 1999.

- [35] M. I. Shliomis and K. I. Morozov. Negative viscosity of ferrofluid under alternating magnetic field. *Physics of Fluids*, 6:2855, 1994.
- [36] J. H. Sánchez and C. Rinaldi. Rotational brownian dynamics simulations of non-interacting magnetized ellipsoidal particles in dc and ac magnetic fields. *Journal of Magnetism and Magnetic Materials*, 321(19):2985–2991, 2009.
- [37] Permeability (electromagnetism). Wikipedia.
- [38] P. Debye. *Polar molecules*, volume 172. Dover New York, 1929.
- [39] Curie temperature. Wikipedia.
- [40] D. Soto-Aquino and C. Rinaldi. Transient magnetoviscosity of dilute ferrofluids. *Journal of Magnetism and Magnetic Materials*, 323(10):1319–1323, 2011.
- [41] J. H. Sánchez and C. Rinaldi. Magnetoviscosity of dilute suspensions of magnetic ellipsoids obtained through rotational brownian dynamics simulations. *Journal of Colloid and Interface Science*, 331(2):500–506, 2009.
- [42] T. A. Franklin. Ferrofluid flow phenomena. Technical report, Massachusetts Institute of Technology, 2003.
- [43] A. Aharoni. Relaxation time of superparamagnetic particles with cubic anisotropy. *Physical Review B*, 7:1103–1107, 1973.
- [44] V. G. Bashtovoi and B. Berkovski. *Magnetic fluids and applications handbook*. Begell House, Incorporated, 1996.
- [45] M. Zahn. *Electromagnetic Field Theory: a problem solving approach*. Krieger Publishing Company, Florida, 1979.
- [46] G. Bierwagen. Next generation of aircraft coatings systems. *Journal of Coatings Technology*, 73(915):45–52, 2001.
- [47] A. J. Vreugdenhil, V. N. Balbyshev, and M. S. Donley. Nanostructured silicon sol-gel surface treatments for al 2024-t3 protection. *Journal of Coatings Technology*, 73(915):35–43, 2001.
- [48] E. A. Starke and J. T. Staley. Application of modern aluminum alloys to aircraft. *Progress in Aerospace Sciences*, 32(2):131–172, 1996.
- [49] NASA. Std-5009, nondestructive evaluation requirements for fracture critical metallic components. *National Aeronautics and Space Administration*, 7, 2008.
- [50] G. I. Nesterenko. Designing the airplane structure for high durability, 2003.
- [51] T. Swift. Fracture analysis of stiffened structure. *Damage Tolerance of Metallic Structures: analysis methods and application*, ASTM STP, 842:69–107, 1984.
- [52] Solenoid. Wikipedia.
- [53] Electromagnet. Wikipedia.

- [54] G. Bates. *Ferromagnetic materials*, edited by ep wohlfarth, 1980.
- [55] D. Martien. Introduction to: ac susceptibility. *Quantum Design, Corporate Headquarters*, 1994.
- [56] G. V. Brown and L. Flax. Superposition of semi-infinite solenoids for calculating magnetic fields of thick solenoids. *Journal of Applied Physics*, 35(6):1764–1767, 1964.

APPENDIXES

APPENDIX A. TABLE OF CONVERSIONS

This appendix shows a table with the units for magnetic properties and conversion factors between SI and CGS systems (Table A.1).

Table A.1: Units for magnetic properties.

Quantity	Symbol	Gaussian	Conversion factor, C^1	SI
Magnetic flux density	B	gauss (G)	10^{-4}	tesla (T)
Magnetic field strength	H	oersted (Oe)	$10^3/4\pi$	A/m
(Volume) magnetization ²	M	emu/cm ³	10^3	A/m
(Volume) magnetization	$4\pi M$	G	$10^3/4\pi$	A/m
Magnetic moment	m	emu, erg/G	10^3	A · m ² , J/T
(Volume) susceptibility	χ	dimensionless	4π	dimensionless
Permeability	μ	dimensionless	$4\pi \times 10^{-7}$	H/m
Relative permeability ³	μ_r	not defined		not defined

¹Multiply a number in Gaussian units by C to convert it to SI (e.g., $1 \text{ G} \times 10^{-4} \text{ T/G} = 10^4 \text{ T}$).

²Magnetic moment per unit volume.

³ $\mu_r = \mu/\mu_0 = 1 + \chi$, all in SI.

APPENDIX B. SPECIFICATIONS OF THE TEST SPECIMEN'S AA

This appendix shows the chemical composition in both weight and atom percentage (Tables B.1 and B.2, respectively) and the mechanical properties (Table B.3) of the DURAL (SAE 2024-T3) and ERGAL (SAE 7075-T6), as provided by the manufacturer.

Table B.1: Chemical composition in weight % of of AA 2024-T3 and AA 7075-T6.

Aluminium alloy	Si	Fe	Cu	Mn	Mg	Zn	Ti	Cr	Others
AA 2024-T3	0.18	0.28	4.46	0.64	1.35	0.04	0.05	0.01	0.01
AA 7075-T6	0.06	0.15	1.50	0.01	2.58	6.00	0.05	0.19	

Table B.2: Chemical composition in atom % of of AA 2024-T3 and AA 7075-T6.

Aluminium alloy	Si	Fe	Cu	Mn	Mg	Zn	Ti	Cr	Others
AA 2024-T3	0.18	0.14	1.95	0.32	1.54	0.02	0.03	0.01	0.00
AA 7075-T6	0.06	0.08	0.67	0.01	2.99	2.59	0.03	0.10	

Table B.3: Mechanical properties of AA 2024-T3 and AA 7075-T6.

Aluminium alloy	Yield stress [MPa]	UTS [MPa]	Elongation [%]	Brinell hardness
AA 2024-T3	377	485	15	123
AA 7075-T6	502	583	12	161

APPENDIX C. INITIAL AND MINIMUM DETECTABLE CRACK SIZES

Figure C.1 shows the assumed initial crack sizes for different types of flaw, whereas Figure C.2 shows the minimum detectable crack sizes for fracture analysis based on standard NDE methods.

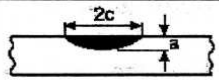
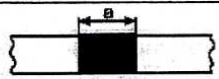
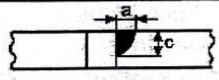
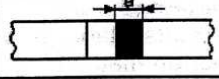
<i>types of flaw</i>		<i>aspect ratio (a/c)</i>	<i>flaw size a (mm) to be assumed immediately after inspection</i>		
<i>description</i>	<i>geometry</i>		<i>pre-service inspection with high standard NDI</i>		<i>In-service inspection with special NDI</i>
			<i>fail-safe</i>	<i>slow flaw growth</i>	
surface flaw		1.0 0.2	1.27	3.18	6.35
through crack			2.54	6.35	12.7
corner flaw at a hole		1.0 0.2	0.51	1.27	6.35 mm beyond fastener head or nut
through crack at a hole			0.51	1.27	6.35 mm beyond fastener head or nut

Figure C.1: USAF MIL-A-83444 safety requirements for assumed initial damage.

Crack Location	Part Thickness, t	Crack Type	Crack Dimension, a	Crack Dimension, c
<u>Eddy Current NDE</u>				
Open Surface	$t \leq 1.27$	Through PTC [†]	t	1.27
	$t > 1.27$		0.51 1.27	2.54 1.27
Edge or Hole	$t \leq 1.91$	Through Corner	t	2.54
	$t > 1.91$		1.91	1.91
<u>Penetrant NDE</u>				
Open Surface	$t \leq 1.27$	Through Through PTC	t	2.54
	$1.27 < t < 1.91$		t	$3.81 - t$
	$t > 1.91$		0.64 1.91	3.18 1.91
Edge or Hole	$t \leq 2.54$	Through Corner	t	3.81
	$t > 2.54$		2.54	3.81
<u>Magnetic Particle NDE</u>				
Open Surface	$t \leq 1.91$	Through PTC	t	3.18
	$t > 1.91$		0.97 1.91	4.78 3.18
Edge or Hole	$t \leq 1.91$	Through Corner	t	6.35
	$t > 1.91$		1.91	6.35
<u>Radiographic NDE</u>				
Open Surface	$t \leq 2.72$ $t > 2.72$	PTC	0.7t	1.91
		PTC	0.7t	0.7t
		Embedded	$2a=0.7t$	0.7t
<u>Ultrasonic NDE</u> Comparable to a Class A Quality Level (ASTM-E-2375)				
Open Surface	$t \geq 2.54$	PTC	0.76	3.81
			1.65	1.65
		Embedded*	0.43 0.99	2.21 0.99

[†] PTC – Partly through crack (Surface Crack)

* Equivalent area is acceptable, ASTM-E-2375 Class A.

Figure C.2: Minimum detectable crack sizes for fracture analysis based on standard NDE methods (in millimeters). See Figure C.1 for definitions of a and c for different geometries. Source: reference [49].

APPENDIX D. CUSTOM-MADE SOLENOID FOR CONDUCTING TESTS

This appendix is structured in four sections: Section D.1. provides the solenoid blueprint and a 3D-view obtained by using a commercial CAD software. Section D.2. provides some pictures of its construction process. Finally, Section D.3. reviews an analytical model found in literature to compute the magnetic field of thick solenoids, whereas Section D.4. presents the theory of magnetic fields produced by alternating current.

D.1. Blueprint and CAD of the solenoid

A commercial CAD software was used to represent the solenoid model. The blueprint with the front, side and top view with corresponding dimensions is shown in Figure D.1, whereas Figure D.2 shows a 3D-view with the external shell set to transparent to ease the visualization of the internal coils.

D.2. Pictures of the solenoid construction process

Figures D.3 to D.5 show the solenoid construction process.

D.3. Analytical model for the DC magnetic field

A model was found in the literature to analytically compute the DC magnetic field inside a thick solenoid by superposition of semi-infinite solenoids [56]. Its procedure is described in the following lines.

The field components of a thick solenoid depend on four variables, which are the radial and axial coordinates of the field point and two parameters needed to specify the solenoid shape, α and β , where

$$\alpha = \frac{\text{outer diameter}}{\text{inner diameter}} \quad (\text{D.1})$$

$$\beta = \frac{\text{length}}{\text{inner diameter}} \quad (\text{D.2})$$

Tabulating this function of four variables would require an unreasonable amount of space for complete coverage of the range of variables of common interest. However, a comprehensive presentation in terms of only two variables is possible if a superposition method is used to find the desired field from tables or graphs of the field of a semi-infinite solenoid with zero inner radius (it differs from ordinary solenoids in that it is semi-infinitely long

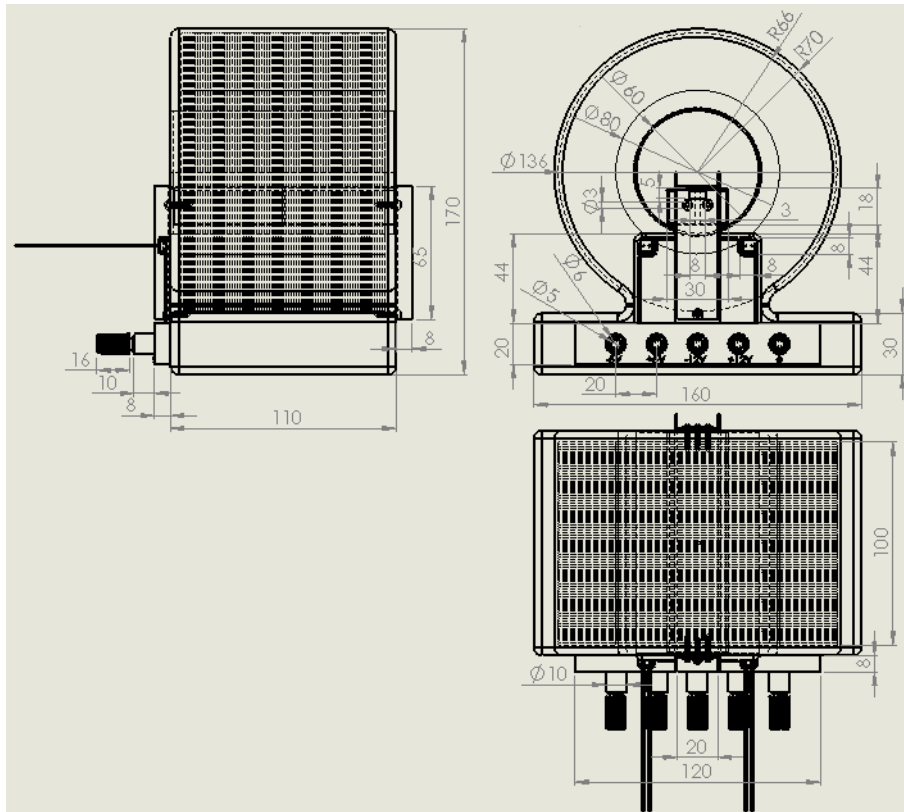


Figure D.1: Custom-made solenoid blueprint.

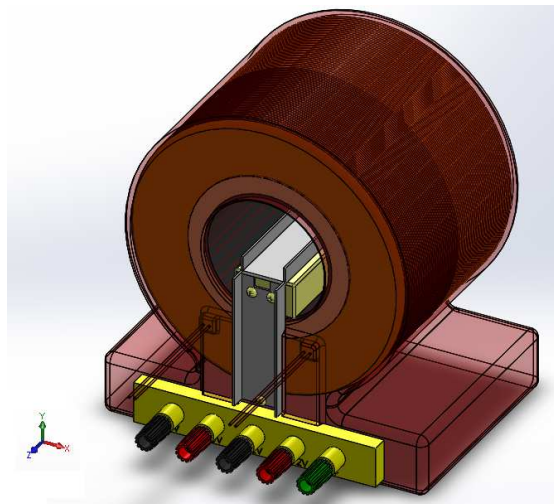


Figure D.2: Trimetric view of the solenoid with transparent shell.

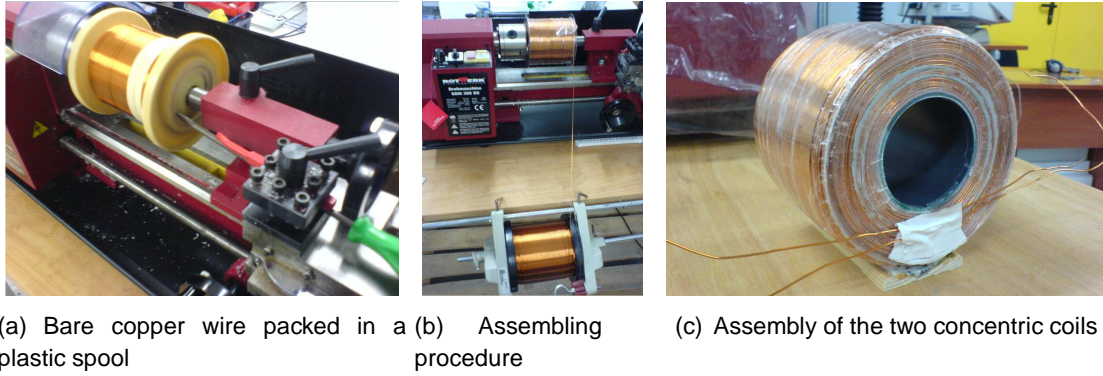


Figure D.3: Coil assembling.

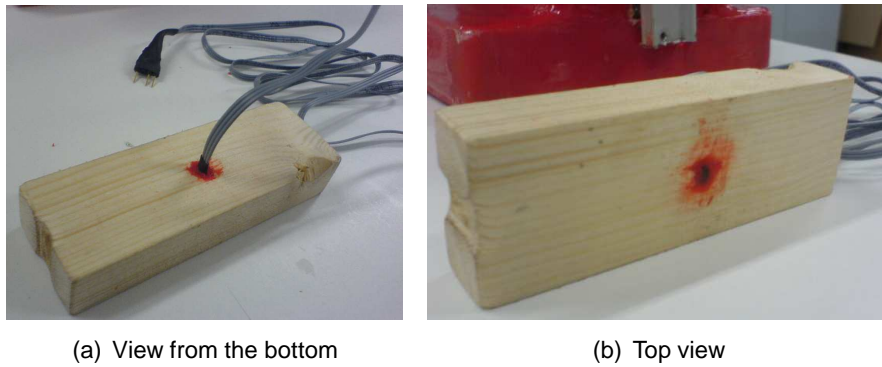


Figure D.4: Sensor location within the support.

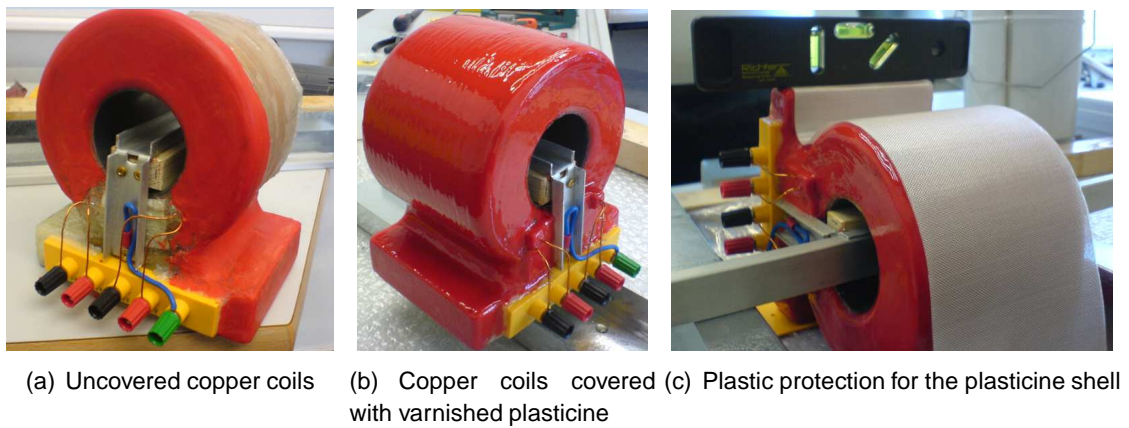


Figure D.5: Custom-made solenoid assembling.

and has no cylindrical hole). The semi-infinite solenoid is defined as an axially symmetric, uniform, azimuthal current density which extends from the axis of a cylindrical coordinate system out to $R = b$ and from $Z = 0$ to $Z = -\infty$ (Fig. D.6).

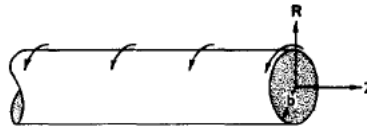


Figure D.6: Semi-infinite solenoid with zero inner radius. Curved arrows indicate direction of current circulation. Source: reference [56]

Each field component of this special solenoid can be expressed non-dimensionally as a function of only two variables, the non-dimensional field-point coordinates,

$$r = R/b \quad (D.3)$$

$$z = Z/b \quad (D.4)$$

Any desired finite solenoid is then treated as a superposition of these semi-infinite solenoids, and any field component is obtained by algebraic addition of four numbers derived from the tables or graphs, each number corresponding to the contribution of one semi-infinite solenoid.

Figure D.7 shows how four semi-infinite solenoids of appropriate sizes and locations can be superimposed to form a thick, finite solenoid. The desired finite solenoid is obtained by cancellation of oppositely directed currents of the different solenoids in many regions.

The field of the thick, finite solenoid can be expressed in terms of the fields of the four contributing semi-infinite solenoids in the following manner. Considering either the axial or the radial component of the field of the infinite solenoid, let H_1, H_2, H_3, H_4 represent the values of the desired field component which would be contributed by the four semi-infinite solenoids. The total field of the desired thick finite solenoid is simply the sum of the contributions of the four semi-infinite solenoids, according to the sense of current densities shown in Figure D.7

$$H = H_1 - H_2 + H_3 - H_4 \quad (D.5)$$

Dividing each term by the current density¹ J (assumed to be uniform) and by the inner radius s of the finite solenoid a non-dimensional expression results

$$\frac{H}{Js} = \frac{H_1}{Js} - \frac{H_2}{Js} + \frac{H_3}{Js} - \frac{H_4}{Js} \quad (D.6)$$

¹The current density J is defined as the ratio of current to wire section, given in units of A/m².

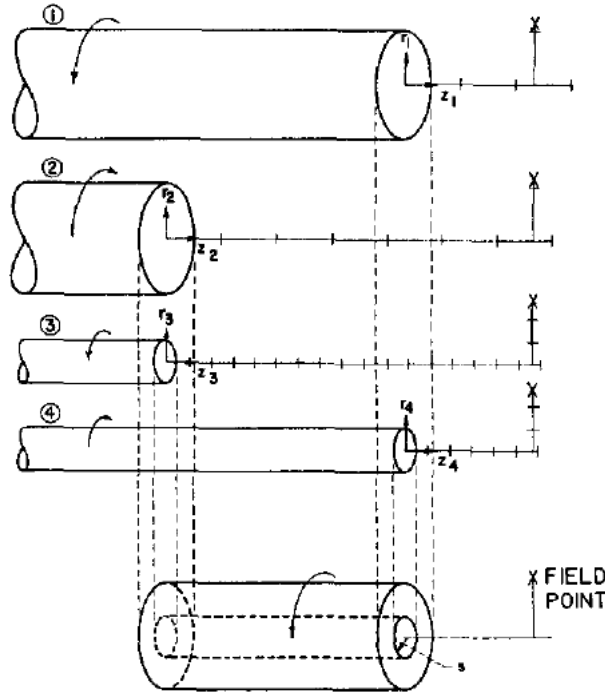


Figure D.7: Formation of a finite solenoid from four semi-infinite solenoids. Note that since non-dimensional tables and graphs are to be used, each semi-infinite solenoid has its own coordinate system, with its own radius as the unit of length. Source: reference [56]

Denoting the radii of the semi-infinite solenoids as b_1 , b_2 , b_3 and b_4 , respectively, and noting that $b_3 = b_4 = s$ and $b_1 = b_2 = \alpha s$, we can write

$$\frac{H}{J_s} = \frac{\alpha H_1}{J b_1} - \frac{\alpha H_2}{J b_2} + \frac{H_3}{J b_3} - \frac{H_4}{J b_4} \tag{D.7}$$

Finally denoting the non-dimensional fields of the four semi-infinite solenoids by H_i/Jb_i by h_i ,

$$\frac{H}{J_s} = \alpha h_1 - \alpha h_2 + h_3 - h_4 \tag{D.8}$$

Since we are interested in the field along the longitudinal axis of the solenoid, the following lines are focused on this component of the field, namely h_z .

As was stated before, a cylindrical coordinate system with its origin at the center of the end face is most convenient. The radial and axial coordinates can be then non-dimensionalized by expressing them in terms of the radius of the semi-infinite solenoid as a unit of measurement. Thus, giving each semi-infinite solenoid its own origin of coordinates and unit of measurement means that the field point to be evaluated will have different coordinates with respect to each of the four semi-infinite solenoids. Figure D.7 shows the coordinate system to be used for each semi-infinite solenoid: (r_i, z_i) for solenoids 1 to 4. Making this field point coordinates explicit in (D.8),

$$\frac{H}{Js} = \alpha h_z(r_1, z_1) - \alpha h_z(r_2, z_2) + h_z(r_3, z_3) - h_z(r_4, z_4) \quad (\text{D.9})$$

Figure D.8 shows the field point within the finite solenoid cross section at which the axial field component is desired.

This non-dimensional field can be approximately evaluated at a certain point $h_z(r, z)$ for each semi-infinite solenoid by using the graph in Figure D.9 with the corresponding non-dimensional values of r and z .

Table D.1 shows the non-dimensional values of r and z used to obtain the contribution of each semi-infinite solenoid to the axial field.

Table D.1: Parameters to obtain the contribution of each semi-infinite solenoid to the axial field.

Quantity	Term	Value
Inner radius	s	0.03 m
Outer radius	$4/3 s$	0.04 m
Semi-infinite solenoid 1	r_1	0
	z_1	-1.25
Semi-infinite solenoid 2	r_2	0
	z_2	1.25
Semi-infinite solenoid 3	r_3	0
	z_3	1.67
Semi-infinite solenoid 4	r_4	0
	z_4	-1.67

The values necessary to compute the total non-dimensional axial field at the desired point are summarized in Table D.2.

Table D.2: Necessary values to compute the total non-dimensional axial field.

Quantity	Term	Value
Shape parameter	α	4/3
Contributions to axial field		
Semi-infinite solenoid 1	h_{z_1}	0.99
Semi-infinite solenoid 2	h_{z_2}	0.038
Semi-infinite solenoid 3	h_{z_3}	0.025
Semi-infinite solenoid 4	h_{z_4}	1

Introducing these values into (D.9) yields

$$\frac{H_z}{Js} = 0.396$$

Finally, to compute the magnetic flux density within the solenoid at the given point, we use

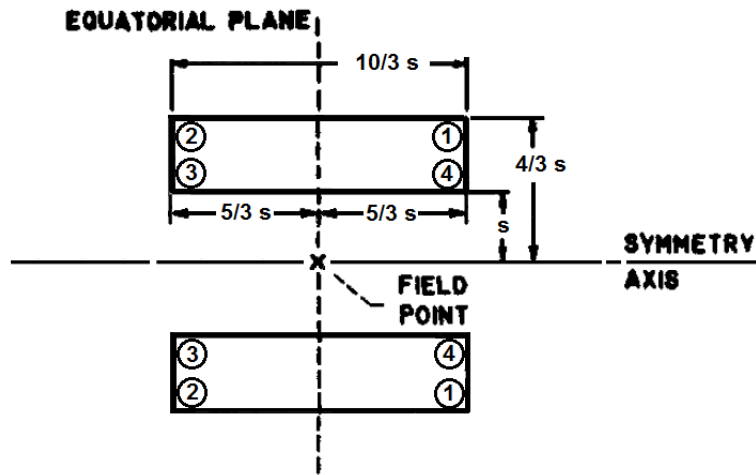


Figure D.8: Cross section of the solenoid's coil #1. Numbered corners correspond to location of the edges of the end planes of the like-numbered semi-infinite solenoids of Figure D.7.

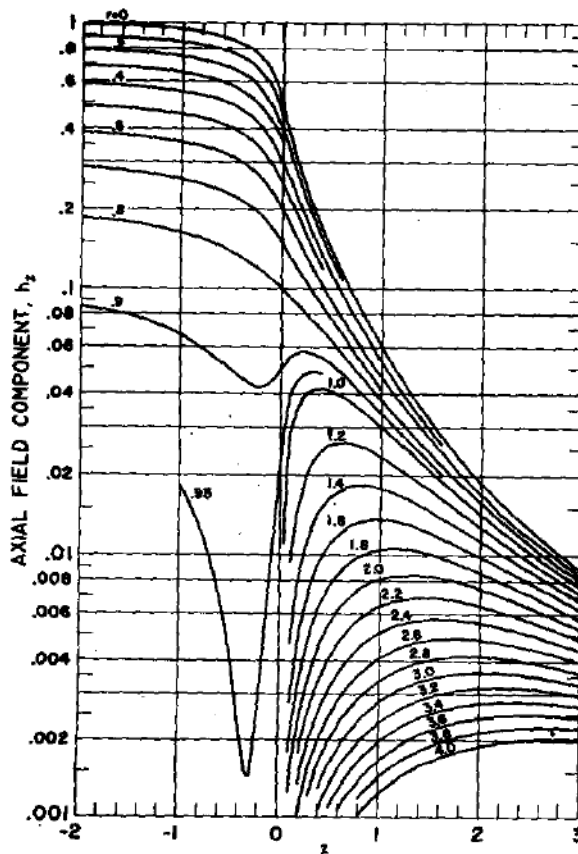


Figure D.9: Non-dimensional axial field of semi-infinite solenoid. Source: reference [56]

$$B_z = \mu_0 H_z = 0.396 \mu_0 J s \quad (\text{D.10})$$

where μ_0 and s are fixed values and J varies with the current. This value of the magnetic flux density is given in SI units, and can be easily converted to Gaussian units (see Appendix A). Figure D.10 shows the theoretical curve of the magnetic field (in Gauss) obtained as a function of the current passing through the solenoid.

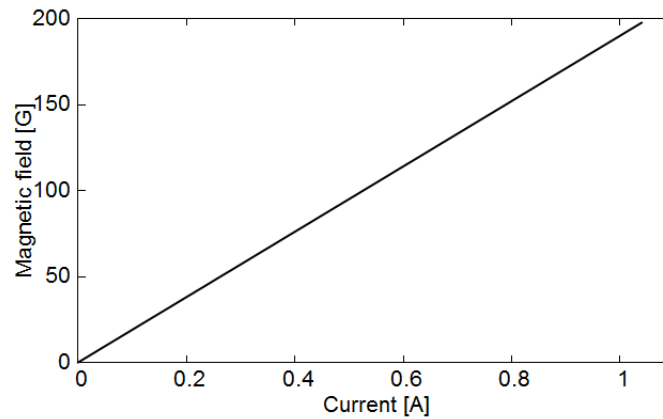


Figure D.10: Theoretical field obtained with coil #1 at the center of the solenoid.

D.4. Magnetic field under alternating current

Considering the solenoid as a series RL circuit (Fig. D.11) the following theory applies.

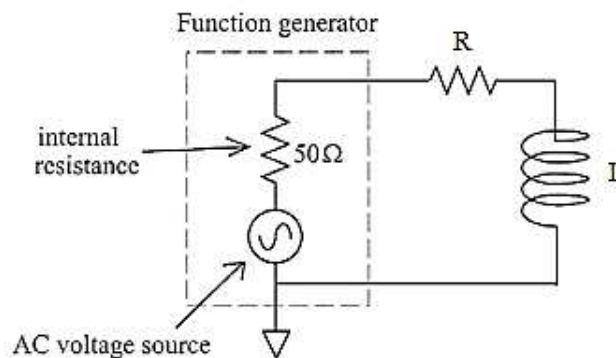


Figure D.11: Series RL circuit diagram.

The complex impedance of this kind of circuit, with a resistance R and inductance L is given by the complex expression

$$Z_L = R + jX_L \quad (\text{D.11})$$

Whereas its modulus, which relates the effective (rms) voltage and current, can be expressed as follows

$$Z_L = \sqrt{R^2 + X_L^2} \quad (\text{D.12})$$

where $X_L = \omega L = 2\pi fL$.

The input tension varies with time and is given by

$$V(t) = V_0 \cos(\omega t) \quad (\text{D.13})$$

While the current writes in the form

$$I(t) = I_0 \cos(\omega t + \varphi) \quad (\text{D.14})$$

where φ is the phase angle that exists between the input tension and current. The phase angle refers to the angle comprised of the resistance R and reactance X_L of equation (D.12), and is computed as follows

$$\varphi = \arctan\left(\frac{X_L}{R}\right) \quad (\text{D.15})$$

While the potential drop across the resistance does not produce any change in phase, the potential drop across the inductor leads the current 90° out of phase with respect to the input tension (Fig. D.12).

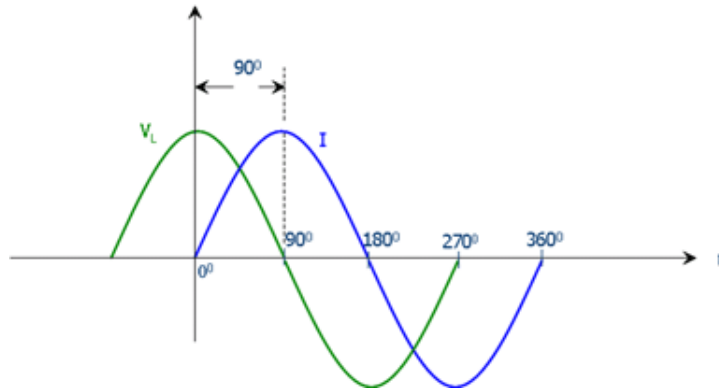


Figure D.12: Phase lag between the current and the input tension in a pure inductive circuit.

This way, the voltage on the solenoid will be largely in quadrature with the current, but not completely, due to coil resistance. According to (D.15), if R and X_L are equal, the phase lag between the tension and the current will be 45° . On the other hand, if R is small relative to the reactance, the phase lag will tend to the 90° of a pure inductive circuit. As a matter of fact, it is important to note that if the frequency is increased so will be the reactance X_L , meaning that at high frequencies the reactance acquires important weight in the circuit. Figure D.13 shows that a phase lag close to 80 degrees exists between the input tension and the measured magnetic field signal, being the latter a function of the current and thus having the same phase.

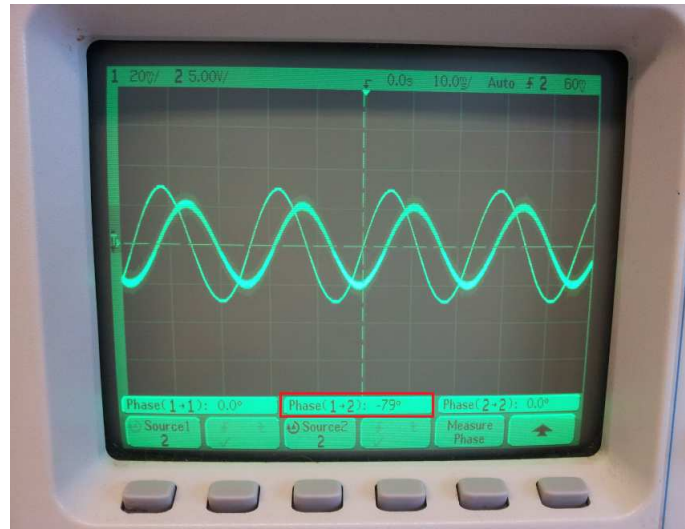


Figure D.13: Phase difference between the magnetic field signal (a function of current) and the input voltage. The value that can be read in the oscilloscope is $\Delta\phi = -79$ deg. The input signal frequency is set to 50 Hz.

Applying Ohm's law, we can write the current as follows,

$$I = \frac{V}{Z} = \frac{V_0}{R + j2\pi fL} \quad (\text{D.16})$$

The magnetic field produced by the solenoid is in phase with the current applied to the coil, as was given previously in (4.3),

$$B = \frac{\mu_0 N}{L} I_0 \cos(\omega t)$$

This means that the field exists in direct relation to the applied current and, if the latter reduces, so does the strength of the field. In the case of a DC solenoid, this phenomenon poses no problems as the current supplied to the coil is of a constant magnitude. The same cannot be said of the AC solenoid, however, as the current constantly cycles between a peak positive voltage, through zero voltage to a peak negative voltage.

The function generator provides an input tension at a constant peak to peak amplitude. For this reason, as the frequency is increased (and thus X_L and, in turn, Z) the current is forced to decrease. Being the produced magnetic field a function of the density of current, if the latter is decreased the former will in turn be decreased (see the response of the coil #1 as a function of the frequency in Figure 4.9).

APPENDIX E. MAGNETOMETER SPECIFICATIONS

This appendix provides detailed information of the *AlphaLab, Inc.* High-Stability DC Magnetometer, regarding its specifications, probe orientation and basic operation. Sensor calibration results obtained by the author are also shown as a verification of the calibration certificate provided by the manufacturer.

E.1. Specifications

The High-Stability DC Magnetometer specifications are listed in Table E.1 below.

Table E.1: *AlphaLab, Inc.* High-Stability DC Magnetometer specifications.

Characteristic	Value
Battery	9 V
Magnetic range	± 199.99 G
Resolution	0.01 G
Temperature range	$-1^{\circ}\text{C} - 43^{\circ}\text{C}$
Frequency range	45 – 2000 Hz
Overall Accuracy	
DC accuracy	$\pm 2\%$
AC accuracy	$\pm 3\%$

E.2. Probe orientation

The actual Hall-type magnetic sensor, with an area of 0.2×0.2 mm, is centered in the rectangular bulge on the top surface at the end of the probe (Fig. E.1).

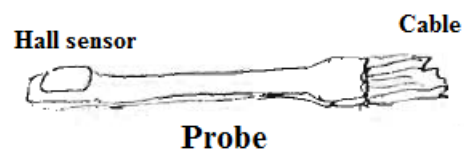


Figure E.1: Scheme of the magnetic probe.

Being magnetic field a vector, it has both a strength and direction. This meter only reads the correct number if the 1-axis probe tip is oriented properly, so that it captures the full field strength¹. Thus, if pointed in the wrong direction, the magnetometer will read less than the full field strength.

¹Technically, Gauss and Tesla are units of *magnetic flux density*, not *magnetic strength*. However, the term *field strength* is used here when talking about Gauss.

Axial vs. transverse measurement

The standard probe is capable of performing measurements perpendicular to the cable direction, i.e., "transverse" measurements, as is shown with the arrow in Figure E.2(a). It can also perform "axial" measurements, which are required when the field direction is parallel to the majority of the cable. This is the case of the present thesis, in which the magnetic field along a solenoid revolution axis is to be measured. To do this, the last part of the probe is to be bent with the bulge facing on the inside of the bend, as shown in Figure E.2(b).

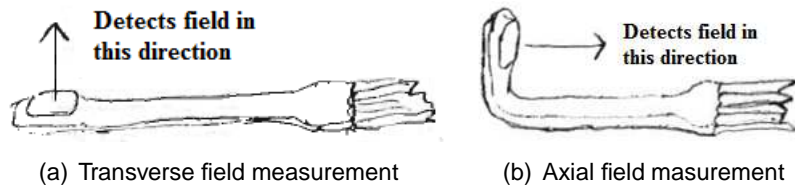


Figure E.2: Probe orientation for field measurement.

Polarity

When the bulge on the probe is pointed toward a south pole of a magnet, the meter reads positive (Fig. E.3); on the contrary, when pointed toward a north pole it reads negative.

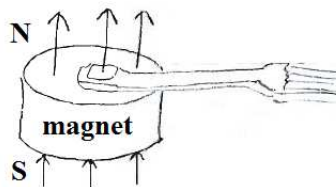


Figure E.3: Schematic of the probe polarity. Meter reads positive in this configuration.

E.3. Basic operation

Once the probe is properly located, the sensor cable must be plugged into the magnetometer box to operate. Choose whether DC or AC magnetic field is to be measured and turn the on/off switch to the "on" position and the meter will display the magnetic field. If the display shows just a "1" or "-1" on the left, it is over range.

Offset

If the existing field is to be cancelled to get a correct zero-field reading on the probe before making measurements, an offset control (aluminum shaft on the top right of the meter box) allows it by adding or subtracting a certain value from the field strength (± 10 G).

E.4. Sensor calibration estimates

A certificate of calibration was provided by the manufacturer when it was acquired in 2007. With a validity of 10 years, until 2017, the completion of the author's master thesis is comprised within this period. As a further verification though, a sensor among the most sensitive and reliable low-field sensors in the industry, with a well-known response to magnetic field variation was used to discard measurement anomalies in the sensed magnetic field and check the linearity of the Hall sensor in the low-field regime: the *Honeywell HMC5883L* three-axis digital compass, which is a surface-mount, multi-chip module designed for low-field magnetic sensing with a digital interface for applications such as low-cost compassing and magnetometry. This sensor is mounted on a *CRIUS MultiWii SE v0.2* board as shown in Figure E.4, along with its axes orientation.

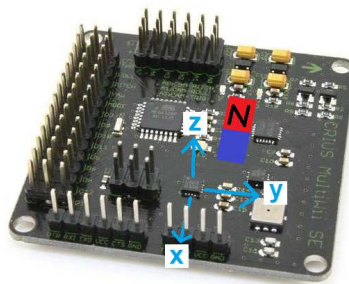


Figure E.4: *Honeywell HMC5883L* axes orientation on *CRIUS MultiWii SE v0.2* board.

The HMC5883L utilizes *Honeywell's* Anisotropic Magnetoresistive technology that provides advantages over other magnetic sensor technologies. This anisotropic, directional sensor features precision in-axis sensitivity and linearity. Its solid-state construction, with very low cross-axis sensitivity, is designed to measure both the direction and the magnitude of Earth's magnetic fields, from milli-gauss to 8 gauss. MultiWii uses Arduino technology so that it can be programmed and implemented as if it were an Arduino board.

The board was placed within the solenoid air gap for magnetic field measurement, right on top of the sample bracket, laying the magnetic sensor approximately in the solenoid center as is the *AlphaLab, Inc.* magnetometer's probe. Several tests were performed and the results are shown Figure E.5. Finally, Figure E.6 shows an average of the achieved data points.

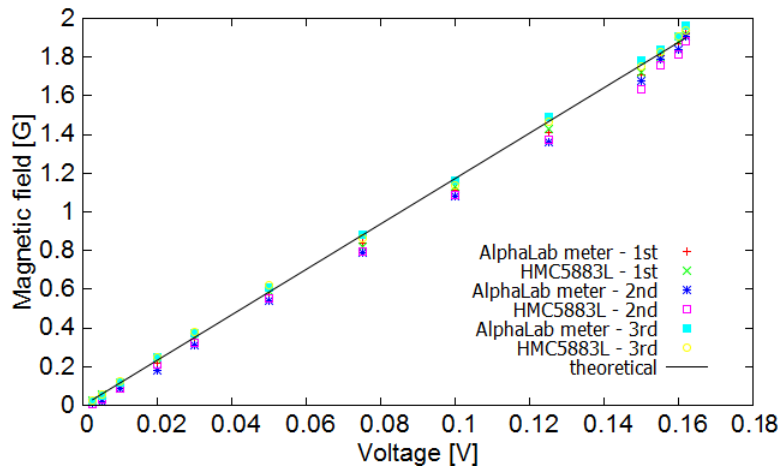


Figure E.5: Low-field magnetic flux density measured with *AlphaLab's* magnetometer and *Honeywell's* HMC5883L. A series of three tests were performed. The theoretical curve is computed from (D.10).

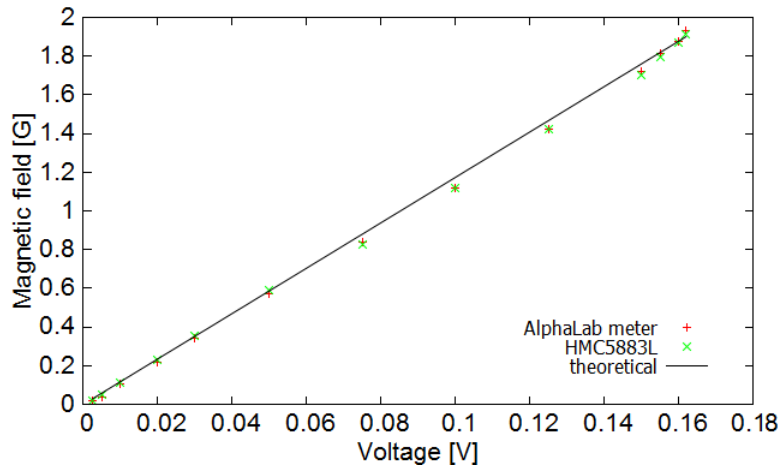


Figure E.6: Average of the low-field magnetic flux density data points measured with *AlphaLab's* magnetometer and *Honeywell's* HMC5883L. The theoretical curve is computed from (D.10).